ASME Journal of Dynamic Systems, Measurement, and Control
Online journal at:
https://asmedigitalcollection.asme.org/dynamicsystems

Global-Position Tracking Control for Multi-Domain Bipedal Walking With Underactuation[1]

Yuan Gao[2]
Department of Mechanical Engineering,
University of Massachusetts,
Lowell, MA 01854
e-mail: Yuan_Gao@student.uml.edu

Kentaro Barhydt[2]
Department of Mechanical Engineering,
Massachusetts Institute of Technology,
Cambridge, MA 02139
e-mail: kbarhydt@mit.edu

Christopher Niezrecki
Department of Mechanical Engineering,
The University of Massachusetts,
Lowell, MA 01851
e-mail: Christopher_Niezrecki@uml.edu

Yan Gu[3]
School of Mechanical Engineering,
Purdue University,
West Lafayette, IN 47907
e-mail: yangu@purdue.edu

Accurate control of a humanoid robot's global position (i.e., its three-dimensional (3D) position in the world) is critical to the reliable execution of high-risk tasks such as avoiding collision with pedestrians in a crowded environment. This paper introduces a time-based nonlinear control approach that achieves accurate global-position tracking (GPT) for multi-domain bipedal walking. Deriving a tracking controller for bipedal robots is challenging due to the highly complex robot dynamics that are time-varying and hybrid, especially for multi-domain walking that involves multiple phases/domains of full actuation, over actuation, and underactuation. To tackle this challenge, we introduce a continuous-phase GPT control law for multi-domain walking, which provably ensures the exponential convergence of the entire error state within the full and over actuation domains and that of the directly regulated error state within the underactuation domain. We then construct sufficient multiple-Lyapunov stability conditions for the hybrid multi-domain tracking error system under the proposed GPT control law. We illustrate the proposed controller design through both three-domain walking with all motors activated and two-domain gait with inactive ankle motors. Simulations of a ROBOTIS OP3 bipedal humanoid robot demonstrate the satisfactory accuracy and convergence rate of the proposed control approach under two different cases of multi-domain walking as well as various walking speed and desired paths.
[DOI: 10.1115/1.4065323]

1 Introduction

Multi-domain walking of legged locomotors refers to the type of walking that involves multiple continuous foot-swinging phases and discrete foot-landing behaviors within a gait cycle, due to changes in foot-ground contact conditions and actuation authority [1,2]. Human walking is a multi-domain process that involves phases with different actuation types. For robotic multi-domain walking, these phases are (1) full actuation phases during which the support foot is flat on the ground and the number of actuators is equal to that of the degrees-of-freedom (DOFs); (2) underactuation phases where the support foot rolls about its toe and the number of actuators is less than that of the DOFs; and (3) over actuation phases within which both feet are on the ground and there are more actuators than DOFs.

Researchers have proposed various control strategies to achieve stable multi-domain walking for bipedal robots. Zhao et al. [2] proposed a hybrid model to capture the multi-domain robot dynamics and used offline optimization to obtain the desired motion trajectory based on the hybrid model. An input-output linearizing control scheme was then applied to drive the robot state to converge to the desired trajectory. The approach was validated on a physical planar bipedal robot, AMBER2, and later extended to another biped platform [1], ATRIAS [3]. Hereid et al. [4] utilized the reduced-order spring loaded inverted pendulum model [5] to design an optimization-based trajectory generation method that plans periodic orbits in the state space of the compliant bipedal robot ATRIAS. The method guarantees orbital stability of the multi-domain gait based on the hybrid zero dynamics (HZD) approach [6]. Reher et al. achieved an energy-optimal multi-domain walking gait on the physical robot platform, DURUS, by creating a hierarchical motion planning and control framework [7]. The framework ensures orbital walking stability and energy efficiency for the multi-domain robot model based on the HZD approach [6]. Hamed et al. [8,9] established orbitally stable multi-domain walking on a quadrupedal robot by modeling the associated hybrid full-order robot dynamics and constructing virtual constraints [10]. While these approaches have realized provable stability and impressive performance of multi-domain walking on various physical robots, it remains unclear how to directly extend them to solve general global-position tracking (GPT) control problems.

In real-world mobility tasks, such as dynamic obstacle avoidance during navigation through a crowded hallway, a robot needs to control its global position accurately with precise timing. Notably, Xiong et al. [11,12] introduced a global-position control framework for underactuated bipedal robots based on a reduced-order hybrid model and orbital stabilization. This approach efficiently plans the desired footstep locations that provably stabilize the desired periodic orbit of a hybrid reduced-order robot model. The controller has enabled versatile and robust underactuated walking on a physical bipedal robot Cassie. Recently, this controller design methodology has been extended to achieve stable multi-domain

[1]This paper was presented at the 2019 DSCC Dynamic Systems and Control Conference.
[2]Yuan Gao and Kentaro Barhydt equally contributed to this paper.
[3]Corresponding author.
Contributed by the Dynamic Systems Division of ASME for publication in the Journal of Dynamic Systems, Measurement, and Control. Manuscript received April 26, 2023; final manuscript received December 22, 2023; published online August 17, 2024. Assoc. Editor: Pranav Bhounsule.

bipedal walking based on a new multi-domain, reduced-order dynamics model [13]. Yet, both the HZD-based approaches [6,14–16] and the reduced-order model based controller frameworks [11–13] utilize orbital stabilization as their underlying stabilization mechanism, which may not ensure reliable tracking of a time trajectory precisely with the desired timing.

We have developed a GPT control approach based on input-output linearization and Lyapunov stability analysis that achieves exponential trajectory tracking for the hybrid model of two-dimensional (2D) fully actuated bipedal walking [17–19]. To extend our approach to 3D fully actuated robots, we considered the robot's lateral global movement and its coupling with forward dynamics through dynamics modeling and stability analysis [20–23]. For fully actuated quadrupedal robotic walking on a rigid surface moving in the inertial frame, we formulated the associated robot dynamics as a hybrid time-varying system and exploited the model to develop a GPT control law for fully actuated quadrupeds [24–26]. However, these methods designed for fully actuated robots cannot solve the multi-domain control problem directly. This is essentially because multi-domain walking involves distinct dynamic behaviors that are significantly more complex than fully actuated walking. Multi-domain walking typically involves under-actuation, and controlling underactuated systems based on input-output linearization is significantly more complex than the input-output linearizing control of fully actuated systems. As shown in our previous study [23], a fully actuated system can be exactly and completely linearized, which allows us to perform the stability analysis of the nonlinear control system based on the well-studied linear system theory. In contrast, an underactuated system may not be exactly and completely linearized. Instead, nonlinear internal dynamics may exist under an input-output linearizing control law, whose stability cannot be directly analyzed based on the linear system theory.

Some of the results presented in this paper have been reported in Ref. [27]. While our previous work in Ref. [27] focused on GPT controller design and stability analysis for hybrid multi-domain models of 2D walking along a straight path, this study extends the previous method to 3D bipedal robotic walking, introducing the following significant new contributions:

(a) Theoretical extension of the previous GPT control method from 2D to 3D multi-domain bipedal robotic walking. The key novelty is the formulation of a new phase variable that represents the distance traveled along a general curved walking path and can be used to encode the desired global-position trajectories along both straight lines and curved paths.
(b) Lyapunov-based stability analysis to generate sufficient conditions under which the proposed GPT control method provably stabilizes 3D multi-domain walking. Full proofs associated with the stability analysis are provided, while only sketches of partial proofs were reported in Ref. [27].
(c) Extension from three-domain walking with all motors activated to two-domain gait with inactive ankle motors, by formulating a hybrid two-domain system and developing a GPT controller for this new gait type. Such an extension was missing in Ref. [27].
(d) Validation of the proposed control approach through simulations of a ROBOTIS OP3 humanoid robot (see Fig. 1) with different types of multi-domain walking, both straight and curved paths, and various desired global-position profiles. In contrast, our previous validation only used a simple 2D biped with seven links [27].
(e) Formulation of the multi-domain control law as a quadratic program (QP) to ensure the feasibility of joint torque limits, and comparison of its performance with an input-output linearizing control law, which were not included in Ref. [27].

This paper is structured as follows: Section 2 explains the full-order robot dynamics model associated with a common three-domain walking gait. Section 3 presents the proposed GPT control law for three-domain walking. Section 4 introduces the Lyapunov-based closed-loop stability analysis. Section 5 summarizes the extension of the controller design from three-domain to two-domain walking. Section 6 reports the simulation validation results. Section 7 discusses the capabilities and limitations of the proposed control approach. Section 8 provides the concluding remarks. Proofs of all theorems and propositions are given in the Appendix.

2 Full-Order Dynamic Modeling of Three-Domain Walking

This section presents the hybrid model of bipedal robot dynamics associated with three-domain walking.

2.1 Coordinate Frames and Generalized Coordinates. This subsection explains the three coordinate frames used in the proposed controller design. Figure 2 illustrates these frames, with the x-, y-, and z-axes, respectively, highlighted in red, green, and blue.

2.1.1 World Frame. The world frame, also known as the inertial frame, is rigidly attached to the ground (see "{World}" in Fig. 2).

2.1.2 Base Frame. The base frame, illustrated as "{Base}" in Fig. 2, is rigidly attached to the robot's trunk. The x-direction (red) points forward, and the z-direction (blue) points toward the robot's head.

2.1.3 Vehicle Frame. The origin of the vehicle frame (see "{Vehicle}" in Fig. 2) coincides with the base frame, and its z-axis remains parallel to that of the world frame. The vehicle frame rotates only about its z-axis by a certain heading (yaw) angle. The yaw angle of the vehicle frame with respect to (w.r.t) the world frame equals that of the base frame w.r.t. the world frame while the roll and pitch angles of the vehicle frame w.r.t the world frame are 0.

2.1.4 Generalized Coordinates. To use Lagrange's method to derive the robot dynamics model, we first introduce the generalized coordinates that represent the base pose and joint angles of the robot.

We use $\mathbf{p}_b \in \mathbb{R}^3$ and $\boldsymbol{\gamma}_b \in \mathrm{SO}(3)$ to respectively denote the absolute base position and orientation w.r.t the world frame, and their coordinates are represented by (x_b, y_b, z_b) and $(\phi_b, \theta_b, \psi_b)$. Here, ϕ_b, θ_b, and ψ_b are the base roll, pitch, and yaw angles, respectively. Then, the 6D pose $\mathbf{q}_b$ of the base is given by $\mathbf{q}_b := \left[\mathbf{p}_b^T, \boldsymbol{\gamma}_b^T\right]^{\mathrm{T}}$.

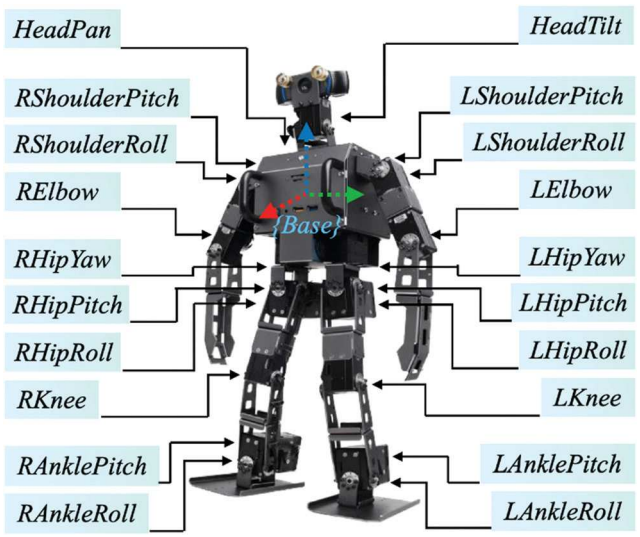

Fig. 1 Illustration of the Darwin OP3 robot, which is used to validate the proposed GPT control approach. Darwin OP3 is a bipedal humanoid robot with twenty revolute joints, designed and manufactured by ROBOTIS Co., Ltd. The reference frame of the robot's floating base, highlighted as "{Base}," is located at the center of the chest.

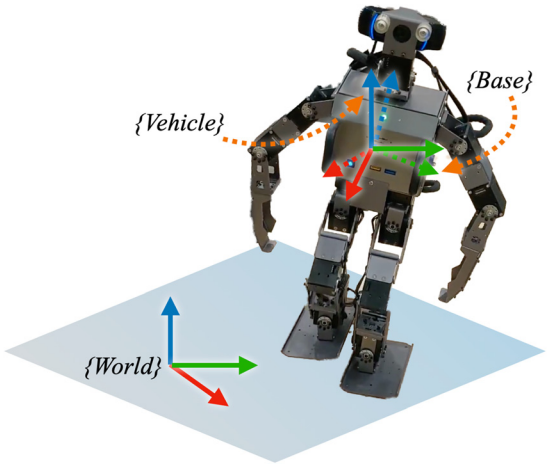

Fig. 2 Illustration of the coordinate frames used in the proposed control design

Let the scalar real variables $q_1, \ldots, q_n$ represent the joint angles of the n revolute joints. Then, the generalized coordinates of a 3D robot, which has a floating base and n independent revolute joints, can be expressed as

$$\mathbf{q} = [\mathbf{q}_b^T, q_1, \ldots, q_n]^{\mathrm{T}} \in \mathcal{Q} \tag{1}$$

where $\mathcal{Q} \subset \mathbb{R}^{n+6}$ is the configuration space.

2.2 Walking Domain Description. For simplicity and without loss of generality, we consider the following assumptions on the foot-ground contact conditions during 3-D walking:

(A1) The toe and heel are the only parts of a support foot that can contact the ground [1].
(A2) While contacting the ground, the toes and/or heels have line contact with the ground.
(A3) There is no foot slipping on the ground.

The assumption of line contact (i.e., assumption (A2)) may present a challenge in the hardware implementation of human-like multi-domain walking that involves support-foot rolling motions. Realizing foot rolling with line contact on hardware can be complex due to the potential foot sliding. To overcome this issue, hardware modifications, particularly in the foot component, are often required. For instance, the design of the AMBER2 bipedal robot [1] is a promising option. Although the underlying theoretical controller design in Ref. [1] prescribes line contact during support-foot rolling about its toe or heel, the hardware design of AMBER2's feet employ a small surface contact at the toe and the heel to prevent foot sliding.

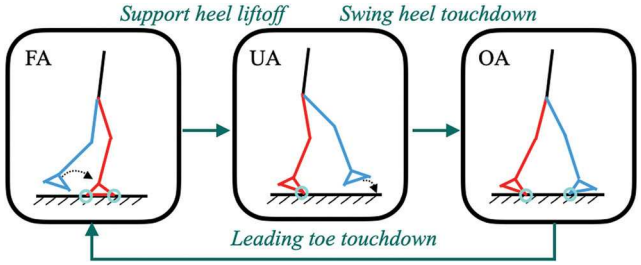

Fig. 3 The directed cycle of 3D three-domain walking. The green circles in the diagram highlight the portions of a foot that are in contact with the ground. The position trajectory of the swing foot is indicated by the dashed arrow. The red and blue legs respectively represent the support and swing legs. Note that when the robot exits the OA domain and enters the FA domain, the swing and support legs switch their roles, and accordingly the leading and trailing legs swap their colors.

Also, we consider the common assumption below about the robot's actuators:

(A4) All the V_O revolute joints of the robot are independently actuated.

Let n_a denote the number of independent actuators, and $n_a = n$ holds under assumption (A4).

Figure 3 illustrates the complete gait cycle of human-like walking with a rolling support foot. As the figure displays, the complete walking cycle involves three continuous phases/domains and three discrete events connecting the three domains. The three domains are:

(i) Full actuation (FA) domain, where n equals the number of DOFs;
(ii) Underactuation (UA) domain, where the number of independent actuators (n) is less than that of the robot's DOFs; and
(iii) Over actuation (OA) domain, where n is greater than the number of DOFs.

The actuation types associated with the three domains are different because those domains have distinct foot-ground contact conditions, which are explained next under assumptions (A1)–(A4).

2.2.1 Full Actuation Domain. As illustrated in the "FA" portion of Fig. 3, only one foot is in support and it is static on the ground within the FA domain. Under assumption (A1), we know both the toe and heel of the support foot contact the ground. From assumptions (A2) and (A3), we can completely characterize the foot-ground contact condition with six independent scalar holonomic constraints. Using n_c to denote the number of holonomic constraints, we have $n_c = 6$ within an FA domain, and the number of DOFs becomes $\mathrm{DOF} = n + 6 - n_c = n$. Meanwhile, $n_a = n$ holds under assumption (A4). Since $\mathrm{DOF} = n_a$, all of the DOFs are directly actuated; that is, the robot is indeed fully actuated.

2.2.2 Underactuation Domain. The "UA" portion of Fig. 3 shows that the robot's support foot rolls about its toe within a UA domain. Under assumptions (A2) and (A3), the number of holonomic constraints is five, i.e., $n_c = 5$. This is because the support foot can only roll about the line toe but its motion is fully restricted in terms of the 3-D translation and the roll and yaw rotation. Then, the number of DOFs is $\mathrm{DOF} = n + 6 - 5 = n + 1$. Since the number of independent actuators, n_a, equals n under assumption (A4) and is lower than the number of DOFs, $(n + 1)$, the robot is underactuated with one degree of underactuation.

2.2.3 Over Actuation Domain. Upon exiting the UA domain, the robot's swing-foot heel strikes the ground and enters the OA domain (Fig. 3). Within an OA domain, both the trailing toe and the leading heel of the robot contact the ground, which is described by ten scalar holonomic constraints (i.e., $n_c = 10$). Thus, the DOF becomes $\mathrm{DOF} = n + 6 - n_c = n - 4$, which is less than the number of actuators under assumption (A4), meaning the robot is over actuated.

2.3 Hybrid Multi-Domain Dynamics. This subsection presents the full-order model of the robot dynamics that corresponds to multi-domain walking. As multi-domain walking involves both continuous- and discrete-time dynamics, a hybrid model is employed to describe the robot dynamics. We first explain the basic components of a typical hybrid system.

2.3.1 Preliminaries on Hybrid Systems. A hybrid control system $\mathcal{HC}$ is a tuple

$$\mathcal{HC} = (\Gamma, D, U, S, \Delta, FG)$$

where

■ The directed circle graph $\Gamma = (V, E)$ comprises a set of vertices $V = \{v_1, v_2, \ldots, v_N\}$ and a set of edges $E = \{e_1, e_2, \ldots, e_N\}$, where N

is the total number of elements in each set. In this paper, each vertex v_i represents the i^{th} domain, while each edge e_i represents the transition from the source domain to the target domain, thereby indicating the ordered sequence of all domains. For three-domain walking, $i = 3$.

- D is a set of domains of admissibility, which are the FA, UA, and OA domains for three-domain walking.
- U is the set of admissible control inputs.
- S is a set of switching surfaces determining the occurrence of switching between domains.
- Δ is a set of reset maps, and the reset map represents the impact dynamics induced by foot touchdown.
- FG is a set of control systems within the domains in D and control inputs in U.

The elements of these sets are explained next.

2.3.2 Continuous-Phase Dynamics. Within any of the three domains, the robot only exhibits continuous movements, and its dynamics model is naturally continuous-time. Applying Lagrange's method, we obtain the second-order, nonlinear robot dynamics as

$$\mathbf{M}(\mathbf{q})\ddot{\mathbf{q}} + \mathbf{c}(\mathbf{q}, \dot{\mathbf{q}}) = \mathbf{B}\mathbf{u} + \mathbf{J}^T\mathbf{F}_c \tag{2}$$

where $\mathbf{M}(\mathbf{q}) : \mathcal{Q} \to \mathbb{R}^{(n+6)\times(n+6)}$ is the inertia matrix. The vector $\mathbf{c} : \mathcal{TQ} \to \mathbb{R}^{(n+6)}$ is the sum of the Coriolis, centrifugal, and gravitational terms, where $\mathcal{TQ}$ is the tangent bundle of $\mathcal{Q}$. The matrix $\mathbf{B} \in \mathbb{R}^{(n+6)\times n_a}$ is the input matrix. The vector $\mathbf{u} \in U \subset \mathbb{R}^{n_a}$ is the joint torque vector. The matrix $\mathbf{J}(\mathbf{q}) : \mathcal{Q} \to \mathbb{R}^{n_c\times(n+6)}$ represents the Jacobian matrix. The vector $\mathbf{F}_c \in \mathbb{R}^{n_c}$ is the constraint force that the ground applies to the foot-ground contact region of the robot. Note that the dimensions of $\mathbf{J}$ and $\mathbf{F}_c$ vary among the three domains due to differences in the ground-contact conditions.

The holonomic constraints can be expressed as

$$\mathbf{J}(\mathbf{q})\ddot{\mathbf{q}} + \dot{\mathbf{J}}(\mathbf{q}, \dot{\mathbf{q}})\dot{\mathbf{q}} = \mathbf{0} \tag{3}$$

Here, $\mathbf{0}$ is a zero vector with an appropriate dimension. With an abuse of notation, we also use $\mathbf{0}$ to represent a zero matrix with a proper dimension in this paper.

Combining Eqs. (2) and (3), we compactly express the continuous-phase dynamics model as [20]

$$\mathbf{M}(\mathbf{q})\ddot{\mathbf{q}} + \bar{\mathbf{c}}(\mathbf{q}, \dot{\mathbf{q}}) = \bar{\mathbf{B}}(\mathbf{q})\mathbf{u} \tag{4}$$

where the vector $\bar{\mathbf{c}}$ and matrix $\bar{\mathbf{B}}$ are defined as $\bar{\mathbf{c}}(\mathbf{q},\dot{\mathbf{q}}) := \mathbf{c} - \mathbf{J}^T(\mathbf{J}\mathbf{M}^{-1}\mathbf{J}^T)^{-1}(\mathbf{J}\mathbf{M}^{-1}\mathbf{c} - \dot{\mathbf{J}}\dot{\mathbf{q}})$ and $\bar{\mathbf{B}}(\mathbf{q}) := \mathbf{B} - \mathbf{J}^T(\mathbf{J}\mathbf{M}^{-1}\mathbf{J}^T)^{-1}\mathbf{J}\mathbf{M}^{-1}\mathbf{B}$.

2.3.3 Switching Surfaces. When a robot's state reaches a switching surface, it exits the source domain and enters the targeted domain. As displayed in Fig. 3, the three-domain walking involves three switching events, which are

(i) Switching from FA to UA ("Support heel liftoff");
(ii) Switching from UA to OA ("Swing heel touchdown"); and
(iii) Switching from OA to FA ("Leading toe touchdown").

The occurrence of these switching events is completely determined by the position and velocity of the robot's swing foot in the world frame as well as the ground-reaction force experienced by the support foot. We use switching surfaces to describe the conditions under which a switching event occurs.

When the heel of the support foot takes off at the end of the FA phase, the robot enters the UA domain (Fig. 3). This support heel liftoff condition can be described using the vertical ground-reaction force applied at the support heel, denoted as $F_{c,z} : \mathcal{TQ} \times U \to \mathbb{R}$. We use $S_{F\to U}$ to denote the switching surface connecting an FA domain and its subsequent UA domain, and express it as

$$S_{F\to U} := \left\{(\mathbf{q}, \dot{\mathbf{q}}, \mathbf{u}) \in \mathcal{TQ} \times U : F_{c,z}(\mathbf{q}, \dot{\mathbf{q}}, \mathbf{u}) \quad = 0\right\}$$

The UA→OA switching occurs when the swing foot's heel lands on the ground (Fig. 3). Accordingly, we express the switching surface that connects a UA domain and its subsequent OA domain, denoted as $S_{U\to O}$, as

$$S_{U\to O} := \left\{(\mathbf{q}, \dot{\mathbf{q}}) \in \mathcal{TQ} : z_{\text{swh}}(\mathbf{q}) = 0,\ \dot{z}_{\text{swh}}(\mathbf{q}, \dot{\mathbf{q}}) < 0\right\}$$

where $z_{\text{swh}} : \mathcal{Q} \to \mathbb{R}$ represents the height of the lowest point within the swing-foot heel above the ground.

As the leading toe touches the ground at the end of an OA phase, a new FA phase is activated (Fig. 3). In this study, we assume that the leading-toe landing and the trailing-foot takeoff occur simultaneously at the end of an OA phase, which is reasonable because the trailing foot typically remains contact with the ground for a brief period (e.g., approximately 3% of a complete human gait cycle [1]) after the touchdown of the leading foot's toe. The switching surface, $S_{O\to F}$, that connects an OA domain and its subsequent FA domain is then expressed as

$$S_{O\to F} := \left\{(\mathbf{q}, \dot{\mathbf{q}}) \in \mathcal{TQ} : z_{\text{swt}}(\mathbf{q}) = 0,\ \dot{z}_{\text{swt}}(\mathbf{q}, \dot{\mathbf{q}}) < 0\right\}$$

where $z_{\text{swt}} : \mathcal{Q} \to \mathbb{R}$ represents the height of the swing-foot toe above the walking surface.

2.3.4 Discrete Impact Dynamics. The complete walking cycle involves two foot-landing impacts; one impact occurs at the landing of the swing-foot heel (i.e., transition from UA to OA) and the other at the touchdown of the leading-foot toe between the OA and FA phases. Note that the switching from FA to UA, characterized by the support heel liftoff, is a continuous process that does not induce any impacts.

We consider the case where the robot's feet and the ground are stiff enough to be considered as rigid, as summarized in the following assumptions [6,28]:

(A5) The landing impact between the robot's foot and the ground is a contact between rigid bodies.
(A6) The impact occurs instantaneously and lasts for an infinitesimal period of time.

Due to the impact between two rigid bodies (assumption (A5)), the robot's generalized velocity $\dot{\mathbf{q}}$ experiences a sudden jump upon a foot-landing impact. Unlike velocity $\dot{\mathbf{q}}$, the configuration $\mathbf{q}$ remains continuous across an impact event as long as there is no coordinate swap of the two legs at any switching event.

Let $\dot{\mathbf{q}}^-$ and $\dot{\mathbf{q}}^+$ represent the values of $\dot{\mathbf{q}}$ just before and after an impact, respectively. The impact dynamics can be described by the following nonlinear reset map [10]:

$$\dot{\mathbf{q}}^+ = \Delta_{\dot{q}}(\mathbf{q})\dot{\mathbf{q}}^- \tag{5}$$

where $\Delta_{\dot{q}} : \mathcal{Q} \to \mathbb{R}^{(n+6)\times(n+6)}$ is a nonlinear matrix-valued function relating the pre-impact generalized velocity $\dot{\mathbf{q}}^-$ to the post-impact one $\dot{\mathbf{q}}^+$. The derivation of $\Delta_{\dot{q}}$ can be found in Ref. [6]. Note that the dimension of $\Delta_{\dot{q}}$ is invariant across the three domains since it characterizes the velocity jumps of all floating-base generalized coordinates.

3 Controller Design for Three-Domain Walking

This section introduces the proposed GPT controller design based on the hybrid model of multi-domain bipedal robotic walking introduced in Sec. 2. The resulting controller provably ensures the exponential error convergence for the directly regulated DOFs within each domain. The sufficient conditions under which the proposed controller guarantees the stability for the overall hybrid system are provided in Sec. 4.

3.1 Desired Trajectory Encoding. As the primary control objective is to provably drive the global-position tracking error to zero, one set of desired trajectories that the proposed controller aims to reliably track is the robot's desired global-position trajectories.

Since a bipedal humanoid robot typically has many more DOFs and actuators than the desired global-position trajectories, the controller could regulate additional variables of interest (e.g., swing-foot pose).

We use both time-based and state-based phase variables to encode these two sets of desired trajectories, as explained next.

3.1.1 Time-Based Encoding Variable. We choose to use the global time variable t to encode the desired global-position trajectories so that a robot's actual horizontal position trajectories in the world (i.e., x_b and y_b) can be accurately controlled with precise timing, which is crucial for real-world tasks such as dynamic obstacle avoidance.

We use $x_d(t)\colon \mathbb{R}^+ \to \mathbb{R}$ and $y_d(t)\colon \mathbb{R}^+ \to \mathbb{R}$ to denote the desired global-position trajectories along the x- and y-axis of the world frame, respectively, and $\psi_d(t)\colon \mathbb{R}^+ \to \mathbb{R}$ is the desired heading direction. We assume that the desired horizontal global-position trajectories $x_d(t)$ and $y_d(t)$ are supplied by a higher-layer planner, and the design of this planner is not the focus of this study. Given $x_d(t)$ and $y_d(t)$, the desired heading direction $\psi_d(t)$ can be designed as a function of $x_d(t)$ and $y_d(t)$, which is $\psi_d(t) := \tan^{-1}(y_d/x_d)$. Such a definition ensures that the robot is facing forward during walking.

We consider the following assumption on the regularity condition of $x_d(t)$ and $y_d(t)$:

(A7) The desired global-position trajectories $x_d(t)$ and $y_d(t)$ are planned as continuously differentiable on $t \in \mathbb{R}^+$ with the norm of $\dot{x}_d(t)$ and $\dot{y}_d(t)$ bounded above by a constant number; that is, there exists a positive constant L_d such that

$$||\dot{x}_d(t)||,\ ||\dot{y}_d(t)|| \le L_d \tag{6}$$

for any $t \in \mathbb{R}^+$.

Under assumption (A7), the time functions $x_d(t)$ and $y_d(t)$ are Lipschitz continuous on $t \in \mathbb{R}^+$ [29], which we utilize in the proposed stability analysis.

3.1.2 State-Based Encoding Variable. As walking inherently exhibits a cyclic movement pattern in the configuration space, it is natural to encode the desired motion trajectories of the robot with a phase variable that represents the walking progress within a cycle.

To encode the desired trajectories other than the desired global-position trajectories, we use a state-based phase variable, denoted as $\theta(\mathbf{q})\colon \mathcal{Q} \to \mathbb{R}$, that represents the total horizontal distance traveled within a walking step. Accordingly, the phase variable $\theta(\mathbf{q})$ increases monotonically within each walking step during straight-line or curved-path walking, which ensures unique mapping from $\theta(\mathbf{q})$ to the encoded desired trajectories. In contrast, in our previous work [18,23], the phase variable is chosen as the walking distance projected along a horizontal straight line, which may not ensure such unique mapping during curved-path walking.

Since the phase variable $\theta(\mathbf{q})$ is essentially the length of a 2D curve that represents the horizontal projection of the 3D walking path on the ground, we can use the actual horizontal velocities ($\dot{x}_b$ and $\dot{y}_b$) of the robot's base to express $\theta(\mathbf{q})$ as

$$\theta(\mathbf{q}(t)) = \int_{t_0}^{t} \sqrt{\dot{x}_b^2(t) + \dot{y}_b^2(t)}\, dt \tag{7}$$

where $t_0 \in \mathbb{R}^+$ represents the actual initial time instant of the given walking step and t is the current time.

The normalized phase variable, which represents the percentage completion of a walking step, is given by

$$s(\theta) := \frac{\theta}{\theta_{\max}} \tag{8}$$

where the real scalar parameter $\theta_{\max}$ represents the maximum value of the phase variable (i.e., the planned total distance to be traveled within a walking step). At the beginning of each step, the normalized phase variable equals 0, while at the end of the step, it equals 1.

The phase variable defined in Eq. (7) is valid for directional bipedal walking but not stepping in place. During stepping in place, the phase variable as defined in Eq. (7) may not monotonically increase as a walking phase progresses. Since the monotonic increase of the phase variable is implicitly required by the proposed approach, as well as the HZD approach [6], the phase variable design in Eq. (7) is not suitable for stepping in place. Toward tracking a stepping-in-place reference, a valid choice of the phase variable is $\theta(t) = \frac{\Delta t}{\Delta \tau}$ [19], where Δt represents how long a walking step has progressed until the given time t and $\Delta\tau$ is the desired duration of the entire step.

3.2 Output Function Design. An output function is a function that represents the difference between a control variable and its desired trajectory, which is essentially the trajectory tracking error. The proposed controller aims to drive the output function to zero for the overall hybrid walking process.

Due to the distinct robot dynamics among different domains, we design different output functions for different domains.

3.2.1 Full Actuation Domain. We use $\mathbf{h}_c^F(\mathbf{q})\colon \mathcal{Q} \to \mathbb{R}^n$ to denote the vector of n control variables that are directly commanded within the FA domain. Without loss of generality, we use the OP3 robot shown in Fig. 1 as an example to explain a common choice of control variables within the FA domain.

The OP3 robot has twenty directly actuated joints (i.e., $n = n_a = 20$) including eight upper body joints. Using n_{up} to denote the number of upper body joints, we have $n_{\text{up}} = 8$.

We choose the twenty control variables as follows:

(i) The robot's global position and orientation represented by the 6D absolute base pose (i.e., position $\mathbf{p}_b$ and orientation γ_b) w.r.t. the world frame;
(ii) The position and orientation of the swing foot w.r.t the vehicle frame, respectively denoted as $\mathbf{p}_{\text{sw}}(\mathbf{q})\colon \mathcal{Q} \to \mathbb{R}^3$ and $\gamma_{\text{sw}}(\mathbf{q})\colon \mathcal{Q} \to \mathbb{R}^3$; and
(iii) The angles of the n_{up} upper body joints, $\mathbf{q}_{\text{up}} \in \mathbb{R}^{n_{\text{up}}}$.

We choose to directly control the global position of the robot to ensure that the robot's base follows the desired global-position trajectory. The base orientation is also directly commanded to guarantee a steady trunk (e.g., for mounting cameras) and the desired heading direction. The swing foot pose is regulated to ensure an appropriate foot posture at the landing event, and the upper body joints are controlled to avoid any unexpected arm motions that may affect the overall walking performance.

The stack of control variables $\mathbf{h}_c^F(\mathbf{q})$ is expressed as

$$\mathbf{h}_c^F(\mathbf{q}) = \begin{bmatrix} x_b \\ y_b \\ \psi_b \\ z_b \\ \phi_b \\ \theta_b \\ \mathbf{p}_{\text{sw}} \\ \gamma_{\text{sw}} \\ \mathbf{q}_{\text{up}} \end{bmatrix} \tag{9}$$

We use $\mathbf{h}_d^F(t,s)\colon \mathbb{R}^+ \times [0,1] \to \mathbb{R}^n$ to denote the desired trajectories for the control variables $\mathbf{h}_c^F(\mathbf{q})$ within the FA domain. These trajectories are encoded by the global time t and the normalized state-based phase variable $s(\theta)$ as follows: (i) the desired trajectories of the base position variables x_b and y_b and the base yaw angle ψ_b are encoded by the global time t, while (ii) those of the other $(n-3)$ control variables (i.e., the base height z_b, base roll angle ϕ_b, base pitch angle θ_b, swing-foot pose $\mathbf{p}_{\text{sw}}$ and γ_{sw}, and upper joint angles $\mathbf{q}_{\text{up}}$) are encoded by the normalized phase variable $s(\theta)$.

The desired trajectory $\mathbf{h}_d^F(t,s)$ is expressed as

$$\mathbf{h}_d^F(t,s) = \begin{bmatrix} x_d(t) \\ y_d(t) \\ \psi_d(t) \\ \boldsymbol{\phi}^F(s) \end{bmatrix} \tag{10}$$

where $x_d(t)$, $y_d(t)$, and $\psi_d(t)$ are defined as in Sec. 3.1.1, and the function $\boldsymbol{\phi}^F(s) : [0,1] \to \mathbb{R}^{n-3}$ represents the desired trajectories of the control variables z_b, ϕ_b, θ_b, ψ_b, $\mathbf{p}_{\text{sw}}$, γ_{sw}, and $\mathbf{q}_{\text{up}}$.

We use Bézier polynomials to parameterize the desired function $\boldsymbol{\phi}^F(s)$ because (i) they do not demonstrate overly large oscillations with relatively small parameter variations and (ii) their expressions at the initial and final instants within a continuous phase are compact [6].

The desired function $\boldsymbol{\phi}^F(s)$ is given by

$$\boldsymbol{\phi}^F(s) := \sum_{k=0}^{M} \boldsymbol{\alpha}_k^F \frac{M!}{k!(M-k)!} s^k (1-s)^{M-k} \tag{11}$$

where $\boldsymbol{\alpha}_k^F \in \mathbb{R}^{n-3}$ ($k \in \{0,1,\ldots,M\}$) is a vector of coefficients of the Bézier polynomials that are to be optimized (Sec. 6), and M is the order of the Bézier polynomials.

The output function during an FA phase is defined as

$$\mathbf{h}^F(t,\mathbf{q}) := \mathbf{h}_c^F(\mathbf{q}) - \mathbf{h}_d^F(t,s) \tag{12}$$

3.2.2 Underactuation Domain. As explained in Sec. 2.2, a robot has $(n+1)$ DOF within the UA domain but only n actuators. Thus, only n (i.e., n) variables can be directly commanded within the UA domain.

We opt to control individual joint angles within the UA domain to mimic human-like walking. By "locking" the joint angles, the robot can perform a controlled falling about the support toe, emulating human walking.

Accordingly, the control variable $\mathbf{h}_c^U(\mathbf{q}) \colon \mathcal{Q} \to \mathbb{R}^n$ is

$$\mathbf{h}_c^U(\mathbf{q}) = \begin{bmatrix} q_1 \\ q_2 \\ q_3 \\ \cdots \\ q_n \end{bmatrix} \tag{13}$$

Let $\mathbf{h}_d^U(s) \colon [0,1] \to \mathbb{R}^n$ denote the desired joint position trajectories within the UA domain. These desired trajectories $\mathbf{h}_d^U(s)$ are parameterized using Bézier polynomials $\boldsymbol{\phi}^U(s) \colon [0,1] \to \mathbb{R}^n$; that is, $\mathbf{h}_d^U = \boldsymbol{\phi}^U(s)$. The function $\boldsymbol{\phi}^U(s)$ can be expressed similar to $\boldsymbol{\phi}^F(s)$.

The associated output function is then given by

$$\mathbf{h}^U(\mathbf{q}) := \mathbf{h}_c^U(\mathbf{q}) - \mathbf{h}_d^U(s) \tag{14}$$

3.2.3 Over Actuation Domain. Let $\mathbf{h}_c^O(\mathbf{q}) \colon \mathcal{Q} \to \mathbb{R}^{n-4}$ denote the control variables within the OA domain. Recall that the robot has n actuators and $(n-4)$ DOFs within the OA domain.

We choose the $(n-4)$ control variables as:

(i) The robot's 6D base pose w.r.t. the world frame;
(ii) The angles of the n_{up} upper body joints, $\mathbf{q}_{\text{up}}$; and
(iii) The pitch angles of the trailing and leading feet, denoted as $\theta_t(\mathbf{q})$ and $\theta_l(\mathbf{q})$, respectively.

Similar to the FA domain, we choose to directly command the robot's 6D base pose within the OA domain to ensure satisfactory global-position tracking performance, as well as the upper-body joint angles to avoid unexpected arm movements that could compromise the robot's balance. Also, regulating the pitch angle of the leading foot helps ensure a flat-foot posture upon switching into the subsequent FA domain where the support foot remains flat on the ground. Meanwhile, controlling the pitch angle of the trailing foot can prevent overly early or late ground contact events.

The control variable $\mathbf{h}_c^O(\mathbf{q})$ is given by

$$\mathbf{h}_c^O(\mathbf{q}) = \begin{bmatrix} x_b \\ y_b \\ \psi_b \\ z_b \\ \phi_b \\ \theta_b \\ \theta_t \\ \theta_l \\ \mathbf{q}_{\text{up}} \end{bmatrix} \tag{15}$$

The desired trajectory $\mathbf{h}_d^O(t,s) \colon \mathbb{R}^+ \times [0,1] \to \mathbb{R}^{n-4}$ within the OA domain is expressed as

$$\mathbf{h}_d^O(t,s) := \begin{bmatrix} x_d(t) \\ y_d(t) \\ \psi_d(t) \\ \boldsymbol{\phi}^O(s) \end{bmatrix} \tag{16}$$

where $\boldsymbol{\phi}^O(s) \colon [0,1] \to \mathbb{R}^{n-4}$ represents the desired trajectories of z_b, ϕ_b, θ_b, θ_t, θ_l, and $\mathbf{q}_{\text{up}}$, which, similar to $\boldsymbol{\phi}^F(s)$ and $\boldsymbol{\phi}^U(s)$, can be chosen as Bézier curves.

The tracking error $\mathbf{h}^O(t,\mathbf{q})$ is then expressed as

$$\mathbf{h}^O(t,\mathbf{q}) := \mathbf{h}_c^O(\mathbf{q}) - \mathbf{h}_d^O(t,s) \tag{17}$$

3.3 Input-Output Linearizing Control. The output functions representing the trajectory tracking errors can be compactly expressed as

$$\mathbf{y}_i = \mathbf{h}^i(t,\mathbf{q}) \tag{18}$$

where the subscript $i \in \{F,U,O\}$ indicates the domain.

Due to the nonlinearity of the robot dynamics and the time-varying nature of the desired trajectories, the dynamics of the output functions are nonlinear and time-varying. To reduce the complexity of controller design, we use input-output linearization to convert the nonlinear time-varying error dynamics into a linear time-invariant system.

Let $\mathbf{u}_i$ ($i \in \{F,U,O\}$) denote the joint torque vector within the given domain. We exploit the input-output linearizing control law [29]

$$\mathbf{u}_i = \left(\frac{\partial \mathbf{h}^i}{\partial \mathbf{q}} \mathbf{M}^{-1} \overline{\mathbf{B}}\right)^{-1} \left[\left(\frac{\partial \mathbf{h}^i}{\partial \mathbf{q}}\right) \mathbf{M}^{-1} \overline{\mathbf{c}} + \mathbf{v}_i - \frac{\partial^2 \mathbf{h}^i}{\partial t^2} - \frac{\partial}{\partial \mathbf{q}} \left(\frac{\partial \mathbf{h}^i}{\partial \mathbf{q}} \dot{\mathbf{q}}\right) \dot{\mathbf{q}}\right] \tag{19}$$

to linearize the continuous-phase output function dynamics in Eq. (4) into $\ddot{\mathbf{y}}_i = \mathbf{v}_i$, where $\mathbf{v}_i$ is the control law of the linearized system. Here, the matrix $\frac{\partial \mathbf{h}^i}{\partial \mathbf{q}} \mathbf{M}^{-1} \overline{\mathbf{B}}$ is invertible on $\mathcal{Q}$ because (i) $\mathbf{M}$ is invertible on $\mathcal{Q}$, (ii) $\frac{\partial \mathbf{h}^i}{\partial \mathbf{q}}$ is full row rank on $\mathcal{Q}$ by design, and (iii) $\overline{\mathbf{B}}$ has full column rank on $\mathcal{Q}$. It should be noted that $\mathbf{u}_i$ has different expressions in different domains, due to the different expressions of the control variables and desired trajectories. For instance, as the output function $\mathbf{h}^U$ is time-independent, the vector $\frac{\partial^2 \mathbf{h}^U}{\partial t^2}$ in Eq. (19) equals zero.

We design $\mathbf{v}_i$ as a proportional-derivative (PD) control law given by

$$\mathbf{v}_i = -\mathbf{K}_{p,i}\mathbf{y}_i - \mathbf{K}_{d,i}\dot{\mathbf{y}}_i \tag{20}$$

where $\mathbf{K}_{p,i}$ and $\mathbf{K}_{d,i}$ are positive-definite diagonal matrices containing the PD control gains, respectively. It is important to note that the dimension of the gains $\mathbf{K}_{p,i}$ and $\mathbf{K}_{d,i}$ depends on that of the output function in each domain; their dimension is $n \times n$ in FA and UA domains, and $(n-4) \times (n-4)$ in the OA domain.

We call the GPT control law in Eqs. (19) and (20) the "IO-PD" controller in the rest of this paper, and the block diagram of the controller is shown in Fig. 4.

With the IO-PD control law, the closed-loop output function dynamics within domain i becomes linear:

$$\ddot{\mathbf{y}}_i = -\mathbf{K}_{d,i}\dot{\mathbf{y}}_i - \mathbf{K}_{p,i}\mathbf{y}_i$$

Drawing upon the well-studied linear systems theory, we can ensure the exponential convergence of $\mathbf{y}_i$ to zero within each domain by properly choosing the values of the PD gain matrices ($\mathbf{K}_{p,i}$ and $\mathbf{K}_{d,i}$) [29].

4 Closed-Loop Stability Analysis for Three-Domain Walking

This section explains the proposed stability analysis of the hybrid closed-loop control system under the continuous IO-PD control law.

The continuous GPT control law introduced in Sec. 3 with properly chosen PD gains achieves exponential stabilization of the output function state within each continuous phase. Yet, the stability of the overall hybrid system is not automatically ensured for two main reasons. First, within the UA domain, the utilization of the input-output linearization technique induces internal dynamics, which the control law cannot directly regulate [19,30]. Second, the impact dynamics in Eq. (5) is uncontrolled due to the infinitesimal duration of the foot-ground impact. As both internal dynamics and reset maps are highly nonlinear and time-varying, analyzing their effects on the system stability is not straightforward.

To ensure stability and satisfactory tracking performance for the overall hybrid closed-loop system, we analyze the closed-loop stability via the construction of multiple Lyapunov functions [31]. The resulting sufficient stability conditions can be used to guide the parameter tuning of the proposed IO-PD law for ensuring system stability and satisfactory tracking.

4.1 Hybrid Closed-Loop Dynamics. This subsection introduces the hybrid closed-loop dynamics under the proposed IO-PD control law in Eqs. (19) and (20), which serves as the basis of the proposed stability analysis.

4.1.1 State Variables Within Different Domains. The state variables of the hybrid closed-loop system include the output function state $\mathbf{y}_i$ and $\dot{\mathbf{y}}_i$ ($i \in \{F, O, \xi\}$). This choice of state variables allows our stability analysis to exploit the linear dynamics of the output function state within each domain, thus greatly reducing the complexity of the stability analysis for the hybrid, time-varying, nonlinear closed-loop system.

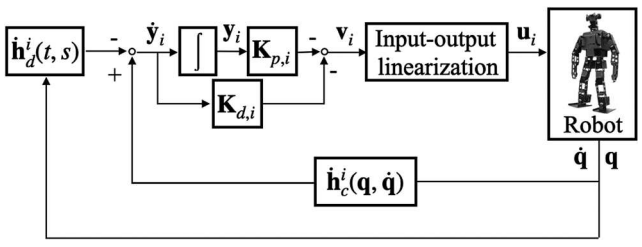

Fig. 4 Block diagram of the proposed GPT control law within each domain. Here $i \in \{F, U, O\}$ indicates the domain type.

We use $\mathbf{x}_F \in \mathbb{R}^{2n}$ and $\mathbf{x}_O \in \mathbb{R}^{2n-8}$ to respectively denote the state within the FA and OA domains, which are exactly the output function state

$$\mathbf{x}_F := \begin{bmatrix} \mathbf{y}_F \\ \dot{\mathbf{y}}_F \end{bmatrix} \text{ and } \mathbf{x}_O := \begin{bmatrix} \mathbf{y}_O \\ \dot{\mathbf{y}}_O \end{bmatrix}$$

Within the UA domain, the output function state, denoted as $\mathbf{x}_\xi \in \mathbb{R}^{2n-2}$, is expressed as

$$\mathbf{x}_\xi := \begin{bmatrix} \mathbf{y}_U \\ \dot{\mathbf{y}}_U \end{bmatrix}$$

Besides $\mathbf{x}_\xi$, the complete state $\mathbf{x}_U$ within the UA domain also includes the uncontrolled state, denoted as $\mathbf{x}_\eta \in \mathbb{R}^2$. Since the stance-foot pitch angle $\theta_{\text{st}}(\mathbf{q})$ is not directly controlled within the UA domain, we define $\mathbf{x}_\eta$ as

$$\mathbf{x}_\eta := \begin{bmatrix} \theta_{\text{st}} \\ \dot{\theta}_{\text{st}} \end{bmatrix}$$

Thus, the complete state within the UA domain is

$$\mathbf{x}_U := \begin{bmatrix} \mathbf{x}_\xi \\ \mathbf{x}_\eta \end{bmatrix} \tag{21}$$

4.1.2 Closed-Loop Error Dynamics. The hybrid closed-loop error dynamics within the FA and OA domains share a similar form, which are given by

$$\begin{cases} \dot{\mathbf{x}}_F = \mathbf{A}_F\mathbf{x}_F & \text{if } (t, \mathbf{x}_F^-) \notin S_{F\to U} \\ \mathbf{x}_U^+ = \boldsymbol{\Delta}_{F\to U}(t, \mathbf{x}_F^-) & \text{if } (t, \mathbf{x}_F^-) \in S_{F\to U} \end{cases}$$
$$\begin{cases} \dot{\mathbf{x}}_O = \mathbf{A}_O\mathbf{x}_O & \text{if } (t, \mathbf{x}_O^-) \notin S_{O\to F} \\ \mathbf{x}_F^+ = \boldsymbol{\Delta}_{O\to F}(t, \mathbf{x}_O^-) & \text{if } (t, \mathbf{x}_O^-) \in S_{O\to F} \end{cases} \tag{22}$$

with

$$\mathbf{A}_F := \begin{bmatrix} \mathbf{0} & \mathbf{I} \\ -\mathbf{K}_{p,F} & -\mathbf{K}_{d,F} \end{bmatrix} \text{ and } \mathbf{A}_O := \begin{bmatrix} \mathbf{0} & \mathbf{I} \\ -\mathbf{K}_{p,O} & -\mathbf{K}_{d,O} \end{bmatrix} \tag{23}$$

where $\mathbf{I}$ is an identity matrix with an appropriate dimension, and $\boldsymbol{\Delta}_{F\to U}: \mathbb{R}^+ \times \mathbb{R}^{2n} \to \mathbb{R}^{2n+2}$ and $\boldsymbol{\Delta}_{O\to F}: \mathbb{R}^+ \times \mathbb{R}^{2n-8} \to \mathbb{R}^{2n}$ are respectively the reset maps of the state vectors $\mathbf{x}_F$ and $\mathbf{x}_O$. The expressions of $\boldsymbol{\Delta}_{F\to U}$ and $\boldsymbol{\Delta}_{O\to F}$ are omitted for space consideration and can be directly obtained by combining the expressions of the reset map $\boldsymbol{\Delta}_{\dot{q}}$ of the generalized coordinates in Eq. (5) and the output functions $\mathbf{y}_F$, $\mathbf{y}_O$, and $\mathbf{y}_U$.

The closed-loop error dynamics associated with the continuous UA phase and the subsequent UA→OA impact map can be expressed as

$$\begin{cases} \begin{cases} \dot{\mathbf{x}}_\xi = \mathbf{A}_\xi\mathbf{x}_\xi \\ \dot{\mathbf{x}}_\eta = \mathbf{f}_\eta(t, \mathbf{x}_\eta, \mathbf{x}_\xi) \end{cases} & \text{if } (t, \mathbf{x}_U^-) \notin S_{U\to O} \\ \mathbf{x}_O^+ = \boldsymbol{\Delta}_{U\to O}\left(t, \mathbf{x}_\xi^-, \mathbf{x}_\eta^-\right) & \text{if } (t, \mathbf{x}_U^-) \in S_{U\to O} \end{cases} \tag{24}$$

where

$$\mathbf{A}_\xi := \begin{bmatrix} \mathbf{0} & \mathbf{I} \\ -\mathbf{K}_{p,U} & -\mathbf{K}_{d,U} \end{bmatrix} \tag{25}$$

The expression of $\mathbf{f}_\eta$ in Eq. (24) can be obtained using the continuous-phase dynamics equation of the generalized coordinates and the expression of the output function $\mathbf{y}_U$. Similar to $\boldsymbol{\Delta}_{F\to U}$ and $\boldsymbol{\Delta}_{O\to F}$, we can readily derive the expression of the reset map $\boldsymbol{\Delta}_{U\to O}$:

$\mathbb{R}^+ \times \mathbb{R}^{2n+2} \to \mathbb{R}^{2n-8}$ based on the reset map in Eq. (5) and the expression of $\mathbf{y}_U$ and $\mathbf{y}_O$.

4.2 Multiple Lyapunov-Like Functions. The proposed stability analysis via the construction of multiple Lyapunov functions begins with the design of the Lyapunov-like functions. We use $V_F(\mathbf{x}_F)$, $V_U(\mathbf{x}_U)$, and $V_O(\mathbf{x}_O)$ to respectively denote the Lyapunov-like functions within the FA, UA, and OA domains, and introduce their mathematical expressions next.

4.2.1 Full Actuation and Over Actuation Domains. As the closed-loop error dynamics within the continuous FA and OA phases are linear and time-invariant, we can construct the Lyapunov-like functions $V_F(\mathbf{x}_F)$ and $V_O(\mathbf{x}_O)$ as [32]

$$V_F(\mathbf{x}_F) = \mathbf{x}_F^T \mathbf{P}_F \mathbf{x}_F \text{ and } V_O(\mathbf{x}_O) = \mathbf{x}_O^T \mathbf{P}_O \mathbf{x}_O$$

with $\mathbf{P}_i$ ($i \in \{F, O\}$) the solution to the Lyapunov equation

$$\mathbf{P}_i \mathbf{A}_i + \mathbf{A}_i^T \mathbf{P}_i = -\mathbf{Q}_i$$

where $\mathbf{Q}_i$ is any symmetric positive-definite matrix with a proper dimension.

4.2.2 Underactuation Domain. As the input-output linearization technique is utilized within the UA domain, internal dynamics exist that cannot be directly controlled [33]. We design the Lyapunov-like function V_U for the UA domain as

$$V_U = V_\xi(\mathbf{x}_\xi) + \beta ||\mathbf{x}_\eta||^2 \tag{26}$$

where $V_\xi(\mathbf{x}_\xi)$ is a positive-definite function and β is a positive constant to be designed.

As the dynamics of the output function state $\mathbf{x}_\xi$ are linear and time-invariant, the construction of $V_\xi(\mathbf{x}_\xi)$ is similar to that of V_F and V_O

$$V_\xi(\mathbf{x}_\xi) = \mathbf{x}_\xi^T \mathbf{P}_\xi \mathbf{x}_\xi$$

where $\mathbf{P}_\xi$ is the solution to the Lyapunov equation

$$\mathbf{P}_\xi \mathbf{A}_\xi + \mathbf{A}_\xi^T \mathbf{P}_\xi = -\mathbf{Q}_\xi$$

with $\mathbf{Q}_\xi$ any symmetric positive-definite matrix with an appropriate dimension.

4.3 Definition of Switching Instants. In the following stability analysis, the three domains of the kth ($k \in \{1, 2, \ldots\}$) walking step are, without loss of generality, ordered as

$$\text{FA} \to \text{UA} \to \text{OA}$$

For the kth walking step, we respectively denote the *actual* values of the initial time instant of the FA phase, the FA $\to$ UA switching instant, the UA $\to$ OA switching instant, and the final time instant of the OA phase as

$$T_{3k-3},\ T_{3k-2},\ T_{3k-1}, \text{ and } T_{3k}$$

The corresponding *desired* switching instants are denoted as

$$\tau_{3k-3},\ \tau_{3k-2},\ \tau_{3k-1}, \text{ and } \tau_{3k}$$

Using these notations, the kth actual complete gait cycle on $t \in (T_{3k-3}, T_{3k})$ comprises

(i) Continuous FA phase on $t \in (T_{3k-3}, T_{3k-2})$;
(ii) FA $\to$ UA switching at $t = T_{3k-2}^-$;
(iii) Continuous UA phase on $t \in (T_{3k-2}, T_{3k-1})$;
(iv) UA $\to$ OA switching at $t = T_{3k-1}^-$;
(v) Continuous OA phase on $t \in (T_{3k-1}, T_{3k})$; and
(vi) OA $\to$ FA switching at $t = T_{3k}^-$.

For brevity, the values of any (scalar or vector) variable $\star$ at $t = T_{3k-j}^-$ and $t = T_{3k-j}^+$, i.e.,

$$\star\left(T_{3k-j}^-\right) \text{ and } \star\left(T_{3k-j}^+\right)$$

are respectively denoted as

$$\star|_{3k-j}^- \text{ and } \star|_{3k-j}^+$$

for any $k \in \{1, 2, \ldots\}$ and $j \in \{0, 1, 2, 3\}$.

4.4 Continuous-Phase Convergence and Boundedness of Lyapunov-Like Functions. As the output function state $\mathbf{x}_i$ ($i \in \{F, O, \xi\}$) is directly controlled, we can readily analyze the convergence of the output functions (and their associated Lyapunov-like functions, V_F, V_O, and V_ξ) within each domain based on the well-studied linear systems theory [29].

PROPOSITION 1. (**Continuous-phase output function convergence within each domain**) *Consider the IO-PD control law in Eqs. (19) and (20), Assumptions (A1)-(A7), and the following condition:*

(B1) *For any $i \in \{F, O, \xi\}$, the PD gains $\mathbf{K}_{p,i}$ and $\mathbf{K}_{d,i}$ are selected such that $\mathbf{A}_i$ is Hurwitz.*

Then, for any $i \in \{F, O, \xi\}$ and any $\mathbf{x}_i \in B_{r_i}(\mathbf{0}) := \{\mathbf{x}_i : ||\mathbf{x}_i|| \le r_i\}$, there exist positive constants r_i, c_{1i}, c_{2i}, and c_{3i} such that the Lyapunov-like function V_i satisfies the following inequalities

$$c_{1i}||\mathbf{x}_i||^2 \le V_i(\mathbf{x}_i) \le c_{2i}||\mathbf{x}_i||^2 \quad \text{and} \quad \dot{V}_i \le -c_{3i} V_i \tag{27}$$

within their respective domains.

Moreover, Eq. (27) yields

$$V_F|_{3k-2}^- \le e^{-c_{3F}(T_{3k-2} - T_{3k-3})} V_F|_{3k-3}^+ \tag{28}$$

$$V_O|_{3k}^- \le e^{-c_{3O}(T_{3k} - T_{3k-1})} V_O|_{3k-1}^+ \tag{29}$$

and

$$V_\xi|_{3k-1}^- \le e^{-c_{3\xi}(T_{3k-1} - T_{3k-2})} V_\xi|_{3k-2}^+ \tag{30}$$

which describe the exponential continuous-phase convergence of V_F, V_O, and V_ξ in their respective domains.

The proof of Proposition 1 is omitted as Proposition 1 is a direct adaptation of the Lyapunov stability theorems from [29]. Note that the explicit relationship between the PD gains and the continuous-phase convergence rates c_{3F}, c_{3O}, and $c_{3\xi}$ can be readily obtained based on Remark 6 of our previous work [23].

Due to the existence of the uncontrolled internal state, the Lyapunov-like function V_U does not necessarily converge within the UA domain despite the exponential continuous-phase convergence of V_ξ guaranteed by the proposed IO-PD control law that satisfies condition (B1). Still, we can prove that within the UA domain of any k^{th} walking step, the value of the Lyapunov-like function V_U just before switching out of the domain, i.e., $V_U|_{3k-1}^-$, is bounded above by a positive-definite function of the "switching-in" value of V_U, i.e., $V_U|_{3k-2}^+$, as summarized in Proposition 2.

PROPOSITION 2. (**Boundedness of Lyapunov-like function within UA domain**) *Consider the IO-PD control law in Eqs. (19) and (20) and all conditions in Proposition 1. There exists a positive real number r_{U1} and a positive-definite function $w_u(\cdot)$ such that*

$$V_U|_{3k-1}^- \le w_u\left(V_U|_{3k-2}^+\right)$$

holds for any $k \in \{1, 2, \ldots\}$ and $\mathbf{x}_U \in B_{r_{U1}}(\mathbf{0})$.

Rationale of proof: The proof of Proposition 2 is given in Appendix A.1. The boundedness of the Lyapunov-like function $V_U(\mathbf{x}_U)$ at $t = T_{3k-1}^-$ is proved based on the definition of $V_U(\mathbf{x}_U)$

given in Eq. (26) and the boundedness of $||\mathbf{x}_U|^-_{3k-1}||$. Recall $\mathbf{x}_U := \begin{bmatrix} \mathbf{x}_\xi^T & \mathbf{x}_\eta^T \end{bmatrix}^T$. We establish the needed bound on $||\mathbf{x}_U|^-_{3k-1}||$ through the bounds on $||\mathbf{x}_\xi|^-_{3k-1}||$ and $||\mathbf{x}_\eta|^-_{3k-1}||$, which are respectively obtained based on the bounds of the continuous-phase dynamics of $\mathbf{x}_\xi$ and $\mathbf{x}_\eta$ and the integration of those bounds within the given continuous UA phase. ■

4.5 Boundedness of Lyapunov-Like Functions Across Jumps. PROPOSITION 3. (**Boundedness across jumps**) *Consider the IO-PD control law in Eqs. (19) and (20), all conditions in Proposition 1, and the following conditions:*

(B2) *The desired trajectories* $\mathbf{h}_d^i$ $(i \in \{F, U, O\})$ *are planned to respect the impact dynamics with a small, constant offset* γ_Δ*; that is*

$$||\boldsymbol{\Delta}_{F\to U}(\tau_{3k-2}, \mathbf{0})|| \le \gamma_\Delta \tag{31}$$

$$||\boldsymbol{\Delta}_{U\to O}(\tau_{3k-1}, \mathbf{0})|| \le \gamma_\Delta, \text{ and} \tag{32}$$

$$||\boldsymbol{\Delta}_{O\to F}(\tau_{3k}, \mathbf{0})|| \le \gamma_\Delta \tag{33}$$

(B3) *The PD gains are chosen to ensure a sufficiently high convergence rate (i.e.,* c_{3F}*,* c_{3O}*, and* $c_{3\xi}$ *in* Eqs. (28)–(30)*) of* V_F*,* V_O*, and* V_ξ*.*

Then, there exists a positive real number r *such that for any* $k \in \{1, 2, \ldots\}$*,* $\mathbf{x}_i \in B_r(\mathbf{0})$ *and* $i \in \{F, U, O\}$*, the following inequalities*

$$\begin{aligned} &\ldots \le V_F|^+_{3k} \le V_F|^+_{3k-3} \le \ldots \le V_F|^+_3 \le V_F|^+_0 \\ &\ldots \le V_U|^+_{3k+1} \le V_U|^+_{3k-2} \le \ldots \le V_U|^+_4 \le V_U|^+_1 \\ &\text{and} \\ &\ldots \le V_O|^+_{3k+2} \le V_O|^+_{3k-1} \le \ldots \le V_O|^+_5 \le V_O|^+_2 \end{aligned} \tag{34}$$

hold; that is, the values of each Lyapunov-like function at their associated "switching-in" instants form a nonincreasing sequence.

Rationale of proof: The proof of Proposition 3 is given in Appendix A.2. The proof shows the derivation details for the first inequality in Eq. (34) (i.e., $V_F|^+_{3k} \le V_F|^+_{3k-3}$ for any $k \in \{1, 2, \ldots\}$), which can be readily extended to prove the other two inequalities.

The proposed proof begins with the analysis of the time evolution of the three Lyapunov-like functions within a complete gait cycle from $t = T^+_{3k-3}$ to $t = T^+_{3k}$, which comprises three continuous phases and three switching events as listed in Sec. 4.3. Specifically, the bounds on the Lyapunov-like functions V_F, V_O, and V_U at the end of their respective continuous phases are given in Propositions 1 and 2, and their bounds at the beginning of those continuous phases are established through the analysis of the reset maps $\boldsymbol{\Delta}_{F\to U}$, $\boldsymbol{\Delta}_{U\to O}$, and $\boldsymbol{\Delta}_{O\to F}$. Finally, we combine these bounds to prove $V_F|^+_{3k} \le V_F|^+_{3k-3}$ under the given conditions. ■

The offset γ_Δ is introduced in condition (B2) for two primary reasons. First, since the system's actual state trajectories inherently possess the impact dynamics, the desired trajectories need to respect the impact dynamics sufficiently closely (i.e., γ_Δ is small enough) [34,35]. If the desired trajectories do not agree with the impact dynamics sufficiently closely, the tracking errors at the beginning of a continuous phase could be overly large even when the errors at the end of the previous continuous phase are small. Such error expansion could induce aggressive control efforts at the beginning of a continuous phase, which could reduce energy efficiency and even cause torque saturation. Second, while it is necessary to enforce the desired trajectories to respect the impact dynamics (e.g., through motion planning), requiring the exact agreement with the highly nonlinear impact dynamics (i.e., $\gamma_\Delta = 0$) could significantly increase the computationally burden of planning, which could be mitigated by allowing a small value of the offset γ_Δ.

4.6 Main Stability Theorem. We derive the stability conditions for the hybrid error system in Eqs. (22) and (24) based on Proposition 3 and the general stability theory via the construction of multiple Lyapunov functions [31].

THEOREM 1. (**Closed-loop stability conditions**) *Consider the IO-PD control law in Eqs. (19) and (20). If all conditions in Proposition 3 are met, the origin of the hybrid closed-loop error system in Eqs. (22) and (24) is locally stable in the sense of Lyapunov.*

Rationale of proof: The full proof of Theorem 1 is given in Appendix A.3. The key idea of the proof is to show that the closed-loop control system satisfies the general multiple-Lyapunov stability conditions given in [31] if all conditions in Proposition 3 are met. ■

5 Extension From Three-Domain Walking With Full Motor Activation to Two-Domain Walking With Inactive Ankle Motors

This section explains the design of a GPT control law for a two-domain walking gait to further illustrate the proposed control approach. The controller is a direct extension of the proposed controller for three-domain walking (with full motor activation). For brevity, this section focuses on describing the distinct aspects of the two-domain design compared to the three-domain case explained earlier.

We consider the case of two-domain walking where underactuation is caused by intentional ankle motor deactivation instead of loss of full contact with the ground as in the case of three-domain walking. Bipedal gait is sometimes intentionally designed as underactuated through motor deactivation at the support ankle [36]. Specifically, by switching off the support ankle motors, the controller can treat the support foot as part of the ground and only handle a point foot-ground contact instead of a finite support polygon, thus simplifying the controller design.

Figure 5 illustrates a complete cycle of a two-domain walking gait, which comprises an FA and a UA domain, with the UA phase induced by intentional motor deactivation. The FA and UA phases share the same foot-ground contact conditions; that is, the toe and heel of the support foot are in a static contact with the ground. Yet, within the UA domain, the ankle-roll and ankle-pitch joints of the support foot are disabled, leading to $\text{DOF} = n_a + 2 > n_a$ (i.e., underactuation).

To differentiate from the case of three-domain walking, we add a "†" superscript to the left of mathematical symbols when introducing the two-domain case.

5.1 Hybrid Robot Dynamics. The continuous-time robot dynamics within the FA domain of two-domain walking have exactly the same expression as those of the three-domain dynamics in Eq. (2).

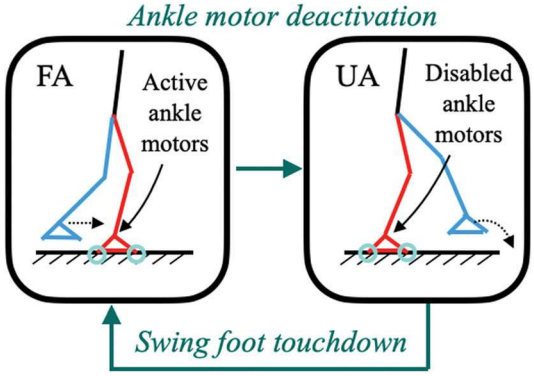

Fig. 5 Illustration of a two-domain gait cycle. The green circles show the portions of the feet that touch the ground. The legs in red and blue are the support and the swing legs, respectively. The dashed arrow shows the motion direction of the swing leg.

The robot dynamics within the UA domain are also the same as Eq. (2) except for the input matrix $\mathbf{B}$ (due to the ankle motor deactivation).

The complete gait cycle contains one foot-landing impact event, which occurs as the robot's state leaves the UA domain and enters the FA domain. The form of the associated impact map is similar to the impact map in Eq. (5) of the three-domain case. For brevity, we omit the expression and derivation details of the impact map.

There are two switching events, F→U and U→F, within a complete gait cycle. The associated switching surfaces, ${}^{\dagger}S_{F\to U}$ and ${}^{\dagger}S_{U\to F}$, are given by

$$
\begin{aligned}
{}^{\dagger}S_{F\to U} &:= \left\{\mathbf{q}\in\mathcal{Q} : \theta(\mathbf{q}) > l_s\right\} \text{ and} \\
{}^{\dagger}S_{U\to F} &:= \left\{(\mathbf{q},\dot{\mathbf{q}})\in\mathcal{TQ} : z_{\text{sw}}(\mathbf{q}) = 0, \dot{z}_{\text{sw}}(\mathbf{q},\dot{\mathbf{q}}) < 0\right\}
\end{aligned}
$$

where $\theta(\mathbf{q})$ is defined as in Eq. (7) and the scalar positive variable l_s represents the desired traveling distance of the robot's base within the FA phase.

5.2 Local Time-based Phase Variable. To allow the convenient adjustment of the intended period of motor deactivation, we introduce a new phase variable ${}^{\dagger}\theta(t)$ for the UA phase representing the elapsed time within this phase: ${}^{\dagger}\theta(t) = t - T_{Uk}$, where T_{Uk} is the initial time instant of the kth UA phase.

The normalized phase variable is defined as ${}^{\dagger}s({}^{\dagger}\theta) := \frac{{}^{\dagger}\theta}{\delta_{\tau_U}}$, where δ_{τ_U} is the expected UA duration. δ_{τ_U} can be treated as a gait parameter that a motion planner adjusts to ensure a reasonable duration of motor deactivation.

5.3 Output Functions. The output function design within the FA domain is the same as the three-domain case.

The control variables within FA, denoted as ${}^{\dagger}\mathbf{h}_c^F(\mathbf{q})$, are chosen the same as the three-domain walking case in Eq. (9). Then, we have ${}^{\dagger}\mathbf{h}_c^F(\mathbf{q}) = \mathbf{h}_c^F(\mathbf{q})$. Accordingly, the desired trajectories ${}^{\dagger}\mathbf{h}_d^F(t,s)$ can be chosen the same as $\mathbf{h}_d^F(t,s)$, leading to the output function expressed as: ${}^{\dagger}\mathbf{h}^F(t,s) = {}^{\dagger}\mathbf{h}_c^F(\mathbf{q}) - {}^{\dagger}\mathbf{h}_d^F(t,s)$.

With two ankle (roll and pitch) motors disabled during the UA phase, the number of variables that can be directly controlled is reduced by two compared to the FA domain. Without loss of generality, we choose the control variables within the UA domain to be the same as the FA domain except that the base roll angle ϕ_b and base pitch angle θ_b are no longer controlled.

The control variables ${}^{\dagger}\mathbf{h}_c^U$ within the UA domain are

$$
{}^{\dagger}\mathbf{h}_c^U(\mathbf{q}) := \begin{bmatrix} x_b \\ y_b \\ \psi_b \\ z_b \\ \mathbf{p}_{\text{sw}}(\mathbf{q}) \\ \boldsymbol{\gamma}_{\text{sw}}(\mathbf{q}) \end{bmatrix} \tag{35}
$$

The desired trajectories ${}^{\dagger}\mathbf{h}_d^U$ are given by

$$
{}^{\dagger}\mathbf{h}_d^U({}^{\dagger}t, {}^{\dagger}s) := \begin{bmatrix} x_d(t) \\ y_d(t) \\ \psi_d(t) \\ {}^{\dagger}\boldsymbol{\phi}^U({}^{\dagger}s) \end{bmatrix} \tag{36}
$$

where ${}^{\dagger}\boldsymbol{\phi}^U({}^{\dagger}s) : [0,1] \to \mathbb{R}^{n_a-5}$ represents the desired trajectories of z_b, $\mathbf{p}_{\text{sw}}$, and $\boldsymbol{\gamma}_{\text{sw}}$.

Then, we obtain the output function ${}^{\dagger}\mathbf{h}^U(t,\mathbf{q})$ as

$$
{}^{\dagger}\mathbf{h}^U(t,\mathbf{q}) := {}^{\dagger}\mathbf{h}_c^U(\mathbf{q}) - {}^{\dagger}\mathbf{h}_d^U({}^{\dagger}t, {}^{\dagger}s) \tag{37}
$$

With the output function ${}^{\dagger}\mathbf{h}^i$ ($i \in \{F, A, U\}$) designed, we can use the same form of the IO-PD control law in Eqs. (19) and (20) and the stability conditions in Theorem 1 to design the needed GPT controller for two-domain walking.

6 Simulation

This section reports the simulation results to demonstrate the satisfactory global-position tracking performance of the proposed control approach.

6.1 Comparative Controller: Input-Output Linearizing Control With Quadratic Programming. This subsection introduces the formulation of the proposed IO-PD controller as a quadratic program (QP) that handles the limited joint-torque capacities of real-world robots, incorporates the realistic friction cone constraint to prevent potential foot slippage, and simultaneously ensures a relatively accurate global-position tracking performance. We refer to the resulting controller as the "IO-QP" controller. Besides enforcing the feasibility constraints and providing tracking performance guarantees, another benefit of the QP formulation lies in its computational efficiency for real-time implementation.

6.1.1 Constraints. To incorporate the friction cone constraint, we explicitly include the ground reaction force $\mathbf{F}_c$ as an optimization variable. Thus, we employ the continuous-phase dynamics model in Eq. (2) together with the holonomic constraint in Eq. (3) to represent the system dynamics in the optimization problem, rather than directly utilizing the effective dynamics model in Eq. (4) that does not contain $\mathbf{F}_c$. This ensures that the presence of $\mathbf{F}_c$ is retained within the formulation. We also consider the IO-PD controller in Eqs. (19) and (20) as an equality constraint.

We use $\mathbf{u}_{\max,i}$ and $\mathbf{u}_{\min,i}$ ($i \in \{F, U, O\}$) to denote the upper and lower limits of the torque command $\mathbf{u}_i$ given in Eq. (19), respectively. Then, the linear inequality constraint that the control signal $\mathbf{u}_i$ should respect can be expressed as $\mathbf{u}_{\min,i} \le \mathbf{u}_i \le \mathbf{u}_{\max,i}$.

To ensure the control command $\mathbf{u}_i$ respects the actuator limits, we incorporate a slack variable $\boldsymbol{\delta}_{QP} \in \mathbb{R}^{n_a}$ in the equality constraint representing the IO-PD controller

$$
\mathbf{u}_i = \mathbf{N}_1(\mathbf{q},\dot{\mathbf{q}}) + \boldsymbol{\delta}_{QP} \tag{38}
$$

where $\mathbf{N}_1 = \left(\frac{\partial \dot{\mathbf{h}}^i}{\partial \mathbf{q}}\mathbf{M}^{-1}\mathbf{B}\right)^{-1}\left[\frac{\partial \dot{\mathbf{h}}^i}{\partial \mathbf{q}}\mathbf{M}^{-1}\ \ \mathbf{c} - \frac{\partial \dot{\mathbf{h}}^i}{\partial \mathbf{q}}\mathbf{M}^{-1}\mathbf{J}^T\mathbf{F}_c\ \ + \mathbf{v}_i - \frac{\partial^2 \mathbf{h}^i}{\partial t^2} - \frac{\partial}{\partial \mathbf{q}}\left(\frac{\partial \dot{\mathbf{h}}^i}{\partial \mathbf{q}}\dot{\mathbf{q}}\right)\dot{\mathbf{q}}\right]$. To avoid overly large deviation from the original control law in Eq. (19), we include the slack variable in the cost function to minimize its norm as explained later.

To enforce the holonomic constraint, the following equality needs to hold:

$$
\mathbf{N}_2(\mathbf{q},\dot{\mathbf{q}}) = \mathbf{0} \tag{39}
$$

where $\mathbf{N}_2 = -\mathbf{J}\mathbf{M}^{-1}\mathbf{c} + \mathbf{J}\mathbf{M}^{-1}\mathbf{B}\mathbf{u}_i + \mathbf{J}\mathbf{M}^{-1}\mathbf{J}^T\mathbf{F}_c + \dot{\mathbf{J}}\dot{\mathbf{q}}$.

Lastly, the friction cone constraint is expressed as

$$
\mathbf{F}_c \in \mathcal{FC} \tag{40}
$$

where $\mathcal{FC}$ represents the linearized friction cone.

6.1.2 Cost Function. The proposed cost function is the sum of two components. One term is $\mathbf{u}_i^T\mathbf{u}_i$ and indicates the magnitude of

Table 1 Mass distribution of the OP3 robot

Body component	Mass (kg)	Length (cm)
Trunk	1.34	63
Left/right thigh	0.31	11
Left/right shank	0.22	11
Left/right foot	0.07	12
Left/right upper arm	0.19	12
Left/right lower arm	0.04	12
Head	0.15	N/A

Table 2 Desired global-position trajectories

Traj. index	$x_d(t)$ (cm)	$y_d(t)$ (cm)	Time interval (s)
(GP1)	$8t$	0	$[0, +\infty)$
(GP2)	$19.1t$	$5.9t$	$[0, +\infty)$
(GP3)	$25t$	0	$[0, 3.13)$
	$3000\sin\left(\frac{t-3.13}{80}\right)+78.2$	$3000\cos\left(\frac{t-3.13}{80}\right)-3000$	$[3.13, 4.25)$
	$24(t-4.25)+120$	$-7(t-4.25)-0.3$	$[4.25, +\infty)$

the control command $\mathbf{u}_i$. Minimizing this term helps guarantee the satisfaction of the torque limit and the energy efficiency of walking.

The other term indicates the weighted norm of the slack variable $\boldsymbol{\delta}_{QP}$, i.e., $p\boldsymbol{\delta}_{QP}^T\boldsymbol{\delta}_{QP}$, with the real positive scalar constant p the slack penalty weight. By including the slack penalty term in the cost function, the deviation of the control signal from the original IO-PD form, which is caused by the relaxation, can be minimized.

It is crucial to point out that the slack variable is not a manually chosen parameter; rather, it is an inherent outcome of the solution generated through the proposed QP. Although we do not directly control the slack variable itself, we do have the flexibility to designate the slack penalty weight p, which dictates how aggressively we seek to minimize the slack variable.

6.1.3 Quadratic Program Formulation. Summarizing the constraints and cost function introduced earlier, we arrive at a QP given by

$$\begin{aligned} \min_{\mathbf{u}_i, \boldsymbol{\delta}_{QP}, \mathbf{F}_c} \quad & \mathbf{u}_i^T\mathbf{u}_i + p\,\boldsymbol{\delta}_{QP}^T\boldsymbol{\delta}_{QP} \\ \text{s.t.} \quad & \mathbf{u}_i = \mathbf{N}_1 + \boldsymbol{\delta}_{QP} \\ & \mathbf{F}_c \in \mathcal{FC} \\ & \mathbf{N}_2 = \mathbf{0} \\ & \mathbf{u}_i \geq \mathbf{u}_{\min,i},\ \mathbf{u}_i \leq \mathbf{u}_{\max,i} \end{aligned} \tag{41}$$

We present validation results for both IO-PD and IO-QP in the following to demonstrate their effectiveness and performance comparison.

6.2 Simulation Setup

6.2.1 Robot Model. The robot used to validate the proposed control approach is an OP3 bipedal humanoid robot developed by ROBOTIS, Inc. (see Fig. 1). The OP3 robot is 50 cm tall and weighs approximately 3.2 kg. It is equipped with 20 actuated revolute joints, as shown in Fig. 1. The mass distribution and geometric specifications of the robot are listed in Table 1. To validate the proposed controller, we use the MATLAB ODE solver `ODE45` to simulate the dynamics models of the OP3 robot for both three-domain walking (Sec. 2) and two-domain walking (Sec. 5). The default tolerance settings of the `ODE45` solver are used.

6.2.2 Desired Global-Position Trajectories and Walking Patterns. As mentioned earlier, this study assumes that the desired global-position trajectories are provided by a higher-layer planner. To assess the effectiveness of the proposed controller, three different desired global-position (GP) trajectories are tested, including single-direction and varying-direction trajectories. These trajectories are specified in Table 2.

The GPs include two straight-line global-position trajectories with distinct heading directions, labeled as (GP1) and (GP2). We set the velocities of (GP1) and (GP2) to be different to evaluate the performance of the controller under different walking speed. To assess the effectiveness of the proposed control law in tracking the desired global-position trajectories along a path with different walking directions, we also consider a walking trajectory (GP3) consisting of two straight-line segments connected via an arc. For the desired horizontal global-position trajectories (GP1) and (GP2) that are straight lines, the desired heading angles are constant and are respectively set as 0 deg and 17.2 deg. For the desired curved-path trajectory (GP3), the desired heading angle changes from 0 deg to 16.3 deg.

The desired functions $\boldsymbol{\phi}^F$, $\boldsymbol{\phi}^U$, and $\boldsymbol{\phi}^O$ are designed as Bézier curves (Sec. 3.2). To respect the impact dynamics as prescribed by condition (B2), their parameters could be designed using the methods introduced in [6]. In our future work, we will optimize the Bézier polynomial coefficients rather than relying on manual tuning to obtain the desired walking patterns. The desired walking patterns corresponding to the desired functions $\boldsymbol{\phi}^F$, $\boldsymbol{\phi}^U$, and $\boldsymbol{\phi}^O$ used in this study are illustrated in Fig. 6. In three-domain walking (lower plot in Fig. 6), the FA, UA, and OA phases take up approximately 33%, 8%, and 59% of one walking step, respectively, while the FA and UA phases of the two-domain walking gait (top plot in Fig. 6) last 81% and 19% of a step, respectively. For both walking patterns, the step length and maximum swing foot height are 7.1 cm and 2.4 cm , respectively.

6.2.3 Simulation Cases. To validate the proposed controller under different desired global-position trajectories, walking patterns, and initial errors, we simulate the following three cases:

(Case A): Combination of desired trajectory (GP1) and two-domain walking pattern (Fig. 6(*a*)).
(Case B): Combination of desired trajectory (GP2) and two-domain walking pattern (Fig. 6(*a*)).
(Case C): Combination of desired trajectory (GP3) and three-domain walking pattern (Fig. 6(*b*)).

Table 3 summarizes the initial tracking error norms for all cases. Note that the initial swing-foot position tracking error is roughly 30–40% of the nominal step length.

6.2.4 Controller Setting. For the IO-PD and IO-QP controllers, the PD controller gains are set as $\mathbf{K}_{p,i} = 225 \cdot \mathbf{I}$ and $\mathbf{K}_{d,i} = 50 \cdot \mathbf{I}$ to ensure the matrix $\mathbf{A}_i$ ($i \in \{F, U, O\}$) is Hurwitz. For the IO-QP controller, the slack penalty weight p (Eq. (41)) is set as $p = 10^7$. This value ensures that the controller is still stabilizing while having enough freedom to satisfy the feasibility constraints. On a computer with an i7 CPU and 32 GB RAM running MATLAB, it takes approximately 1 ms to solve the QP problem in Eq. (41).

To verify the stability of the multi-domain walking system, we construct the three Lyapunov-like functions V_F, V_U, and V_O as introduced in Sec. 4. In all domains, the matrix $\mathbf{P}_i$ ($i \in \{F, \xi, O\}$) is obtained by solving the Lyapunov equation using the gain matrices $\mathbf{K}_{p,i}$ and $\mathbf{K}_{d,i}$ and the matrix $\mathbf{Q}_i$. Without loss of generality, we choose $\mathbf{Q}_i$ as an identity matrix. For the UA phase, the value of β in the definition of V_U in Eq. (26) is set as 0.001.

6.3 Simulation Results. This subsection presents the tracking results of our proposed IO-PD and IO-QP controllers under Cases A-C. The simulation video is available online.[4]

6.3.1 Global-Position Tracking Performance. Figures 7 and 8 show the tracking performance of the proposed IO-PD and IO-QP controllers under Cases A and B, respectively. As explained earlier, Cases A and B share the same desired walking pattern of two-domain walking, but they have different desired global-position trajectories and initial errors. For both cases, the IO-PD and IO-QP

[4] https://youtu.be/IfvYfRlNXHI

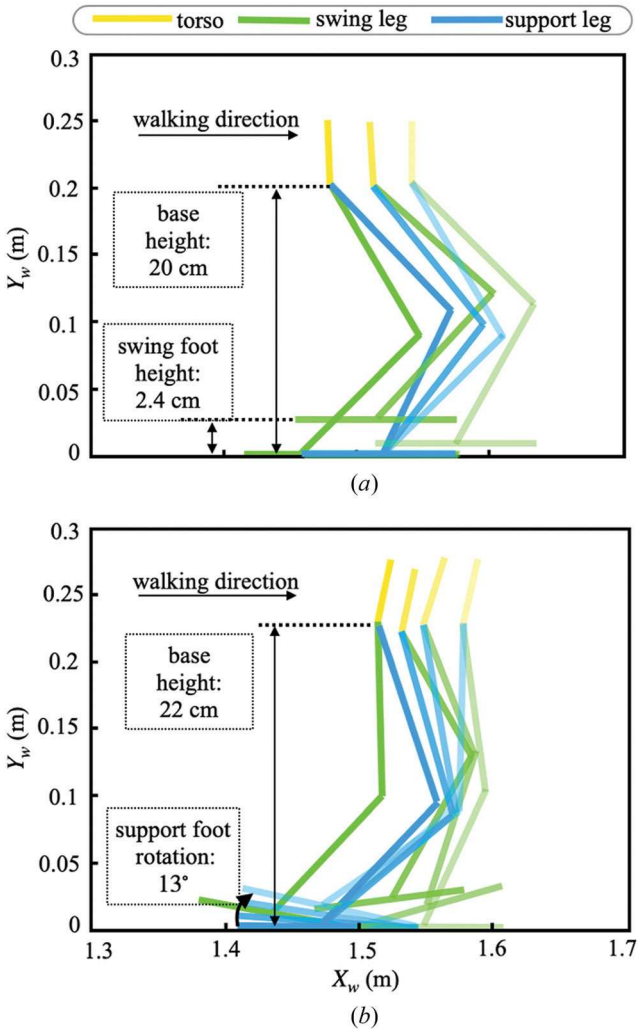

Fig. 6 Desired walking patterns for (*a*) two-domain walking (Cases A and B) and (*b*) three-domain walking (Case C) in the sagittal plane. The labels X_W and Y_W represent the *x*- and *y*-axes of the world frame, respectively.

Table 3 Initial tracking error norms for three cases

Tracking error norm	Case A	Case B	Case C
Swing foot position (% of step length)	27.5	27.5	40
Base orientation (deg)	0	17	12
Base position (% of step length)	15	15	8

controllers satisfactorily drive the robot's actual horizontal global position (x_b, y_b) to the desired trajectories $(x_d(t), y_d(t))$, as shown in the top four plots in each figure. Also, from the footstep locations displayed at the bottom of each figure, the robot is able to walk along the desired walking path over the ground. In particular, the footstep trajectories in Fig. 8 demonstrate that even with a notable initial error (approx. 17 deg) of the robot's heading direction, the robot is able to quickly converge to the desired walking path.

Figure 9 displays the global-position tracking results of three-domain walking for Case C (see Fig. 10 for visual illustration). The top two plots, i.e., the time profiles of the forward and lateral base position (x_b and y_b), show that the actual horizontal global position diverges from the reference within the UA phase during which the global position is not directly controlled. Despite the error divergence within the UA phase, the actual global-position error still converges to close to zero over the entire walking process thanks to convergence within the FA and OA domains, confirming the validity of Theorem 1.

The video clearly illustrates that the robot's heading direction is closely aligned with that of the desired walking path (as specified in Sec. 6.2.2) throughout the walking process. In Cases A and B, the robot's heading direction angles are respectively close to the desired angles of 0 deg and 17.2 deg throughout the test cases. In Case C, as the desired heading angle changes from 0 deg to 16.3 deg, the actual heading angle also increases from around 0 deg to approximately 16.0 deg.

6.3.2 Convergence of Lyapunov-Like Functions. The Lyapunov-like functions under the IO-PD and IO-QP control laws for Case C are illustrated in Fig. 11. Both control laws ensure the continuous-phase convergence of V_F and V_O satisfies condition (B1). Although V_U diverges during the UA phase, it remains bounded and satisfies condition (B3). Moreover, the desired trajectories parameterized as Bézier curves are planned to satisfy (B2). Thus, the Lyapunov-like functions behave as predicted by

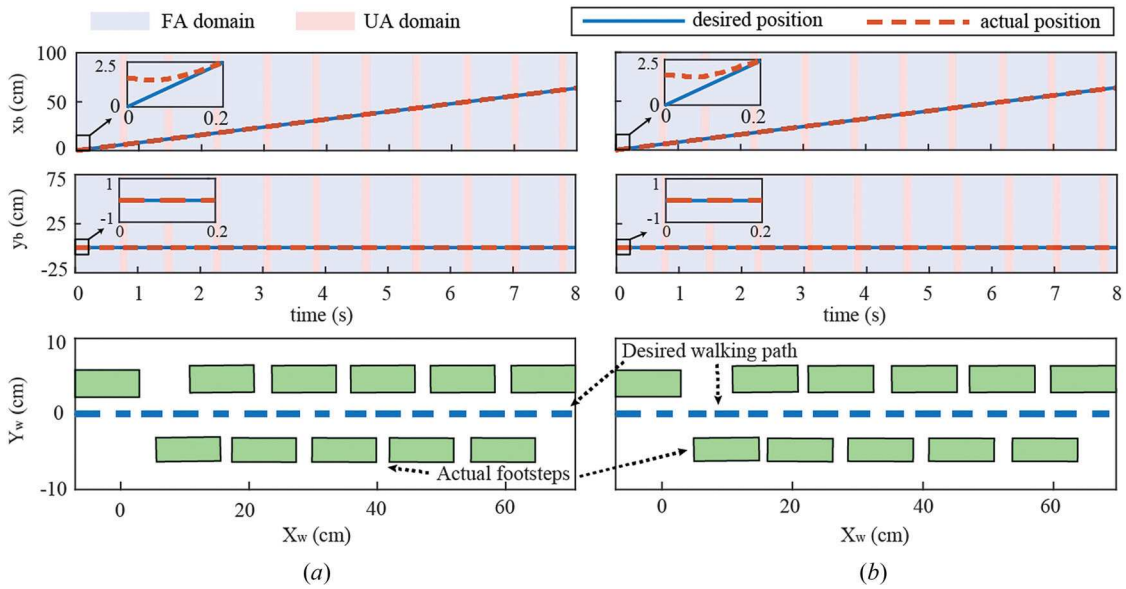

Fig. 7 Satisfactory global-position tracking performance under Case A. The top row shows the global-position tracking results, and the bottom row displays the straight-line desired walking path and the actual footstep locations. The initial errors are listed in Table 3. (*a*) IO-PD and (*b*) IO-QP.

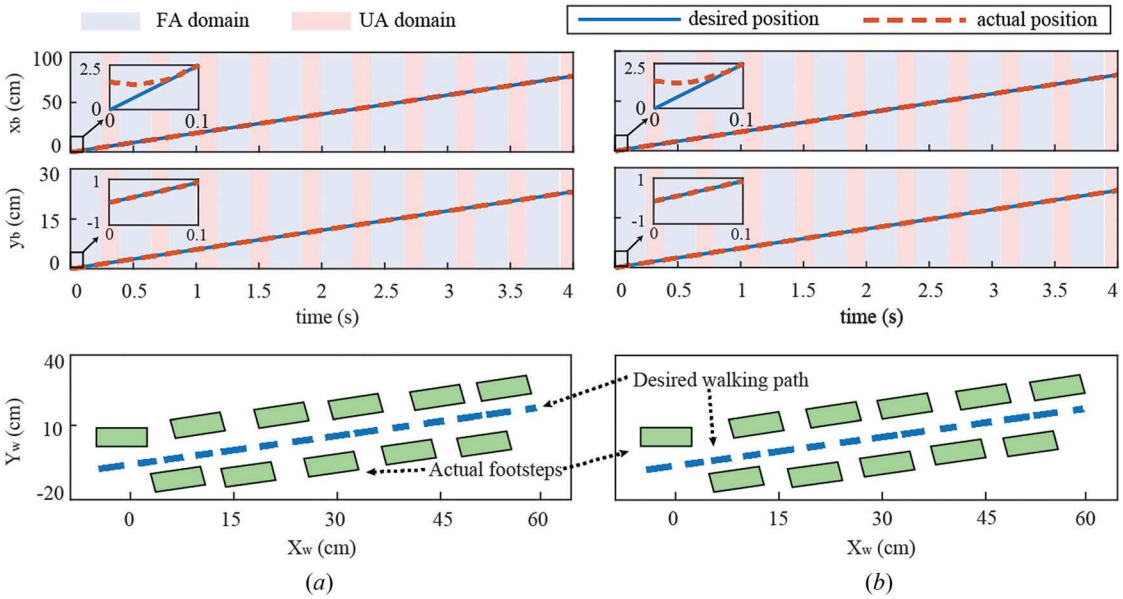

Fig. 8 Satisfactory global-position tracking performance under Case B. The top row shows the global-position tracking results, and the bottom row displays the desired straight-line walking path and the actual footstep locations. The initial errors are listed in Table 3. (*a*) IO-PD and (*b*) IO-QP.

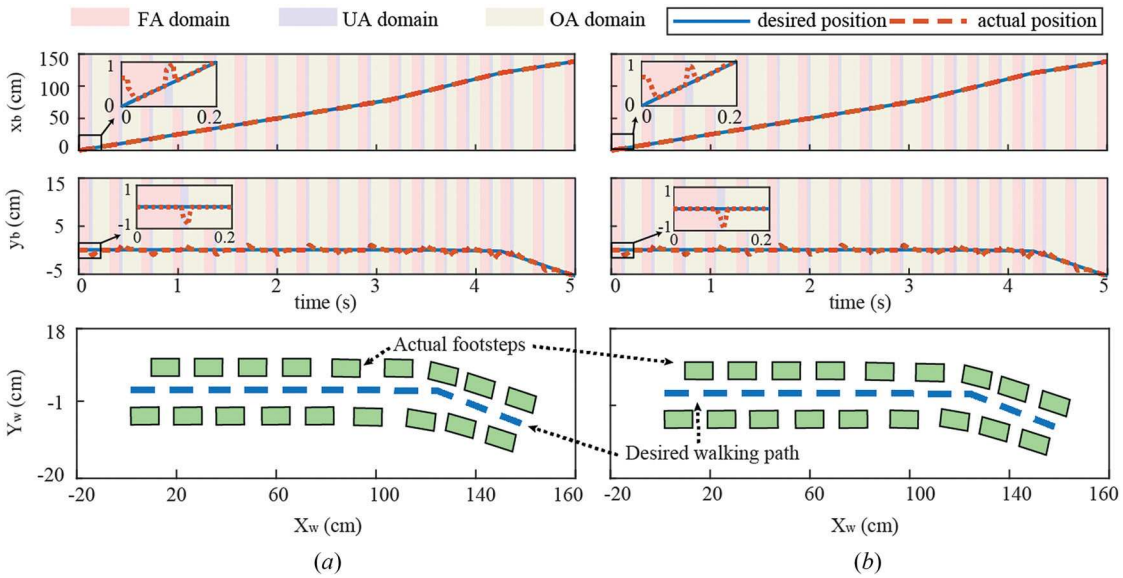

Fig. 9 Satisfactory global-position tracking performance under Case C. The top row shows the global-position tracking results, and the bottom row displays the desired walking path and the actual footstep locations. The desired walking path consists of two straight lines connected by an arc. The initial errors are listed in the Table 3. (*a*) IO-PD and (*b*) IO-QP.

conditions (C1)–(C3) in the proof of Theorem 1, indicating closed-loop stability.

6.3.3 Satisfaction of Torque Limits. Figure 12 illustrates the joint torque profiles of each leg motor under the IO-PD and IO-QP control methods for Case B. The torque limits $u_{\max,i}$ and $u_{\min,i}$ ($i \in \{F, U, O\}$) are set as 4.1 N and −4.1 N, respectively. It is observed that the torque experiences sudden spikes due to the foot-landing impact at the switching from the UA to the FA phases. Due to the notable initial tracking errors, there are also multiple spikes in the joint torques at the beginning period of the entire walking process. These spikes tend to be more significant with the IO-PD controller than with the IO-QP controller. In fact, all of the torque peaks under IO-QP are within the torque limits whereas some of those peaks under IO-PD exceed the limits. This is because the IO-QP controller explicitly enforces the torque limits but IO-PD does

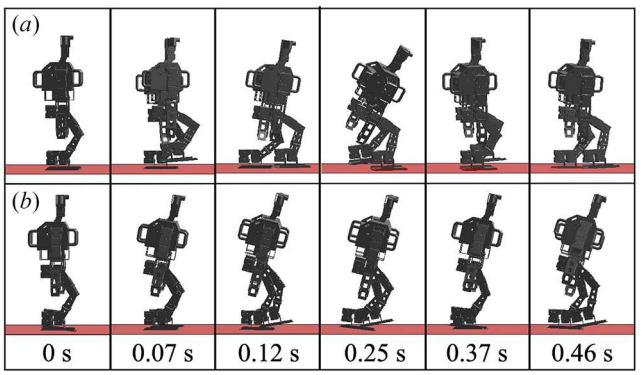

Fig. 10 Time-lapse figures of OP3 walking in MATLAB simulations: (*a*) two-domain walking and (*b*) three-domain walking

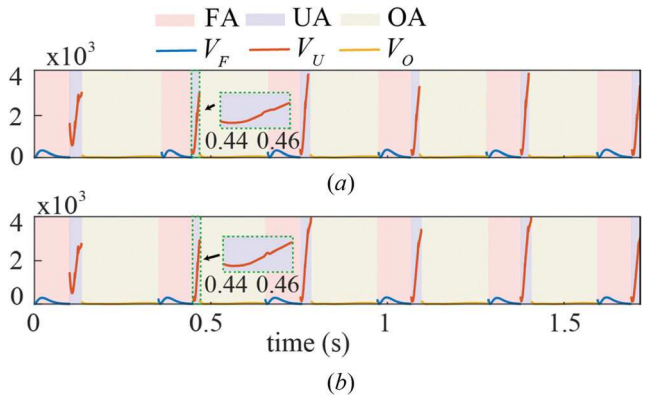

Fig. 11 Time evolutions of multiple Lyapunov-like functions under Case C. The closed-loop stability is confirmed by the behaviors of the multiple Lyapunov functions, which complies with conditions (C1)–(C3) stated in the proof of Theorem 1 for both (*a*) IO-PD and (*b*) IO-QP control laws.

not. This comparison highlights the advantage of using IO-QP over IO-PD in ensuring satisfaction of actuation constraints.

6.3.4 Additional Webots Simulation Results. To gain preliminary insights into the potential hardware implementation of the proposed control approach, 3D realistic simulations in Webots are performed, with the results shown in Fig. 13. The figure illustrates the global-position tracking performance and the associated ankle joint torque profiles for two-domain walking in Webots. The desired global-position trajectory in the forward direction is $x_d(t) = 4.4t - 3$ (cm). As the plot reveals, despite a nonzero initial tracking error, the global-position tracking error is within an acceptable small bound. The robot initiates its motion with its right leg, and it is noteworthy to observe the zero support-ankle torque during the underactuated phase caused by ankle motor de-activation. Also, the percentage of the underactuation phase for the two-domain walking is approximately 16%. This is considerably longer than the three-domain walking results (8%), and comparable to human-like walking [1] during which the underactuation phase constitutes around 18% of a gait cycle.

7 Discussion

This study has introduced a nonlinear GPT control approach for 3D multi-domain bipedal robotic walking based on hybrid full-order dynamics modeling and multiple Lyapunov stability analysis. Similar to the HZD-based approaches [4,8,37] for multi-domain walking, our controller only acts within continuous phases, leaving the discrete impact dynamics uncontrolled. Another key similarity lies in that we build the controller based on the hybrid, nonlinear, full-order dynamics model of multi-domain walking that faithfully captures the true robot dynamics and we exploit the input-output linearization technique to exactly linearize the complex continuous-phase robot dynamics.

Despite these similarities, our control law focuses on accurately tracking the desired global-position trajectories with precise timing, whereas the HZD-based approach may not be directly extended to achieve such global-position tracking performance. This is essentially due to the different stability types that the two approaches impose. The stability conditions proposed in this study enforce the stability of the desired global-position trajectory, which is a time function encoded by the global time. In contrast, the stability conditions underlying the HZD framework ensure the stability of the desired periodic orbit, which is a curve in the state space on which infinitely many global-position trajectories reside. Similar to the

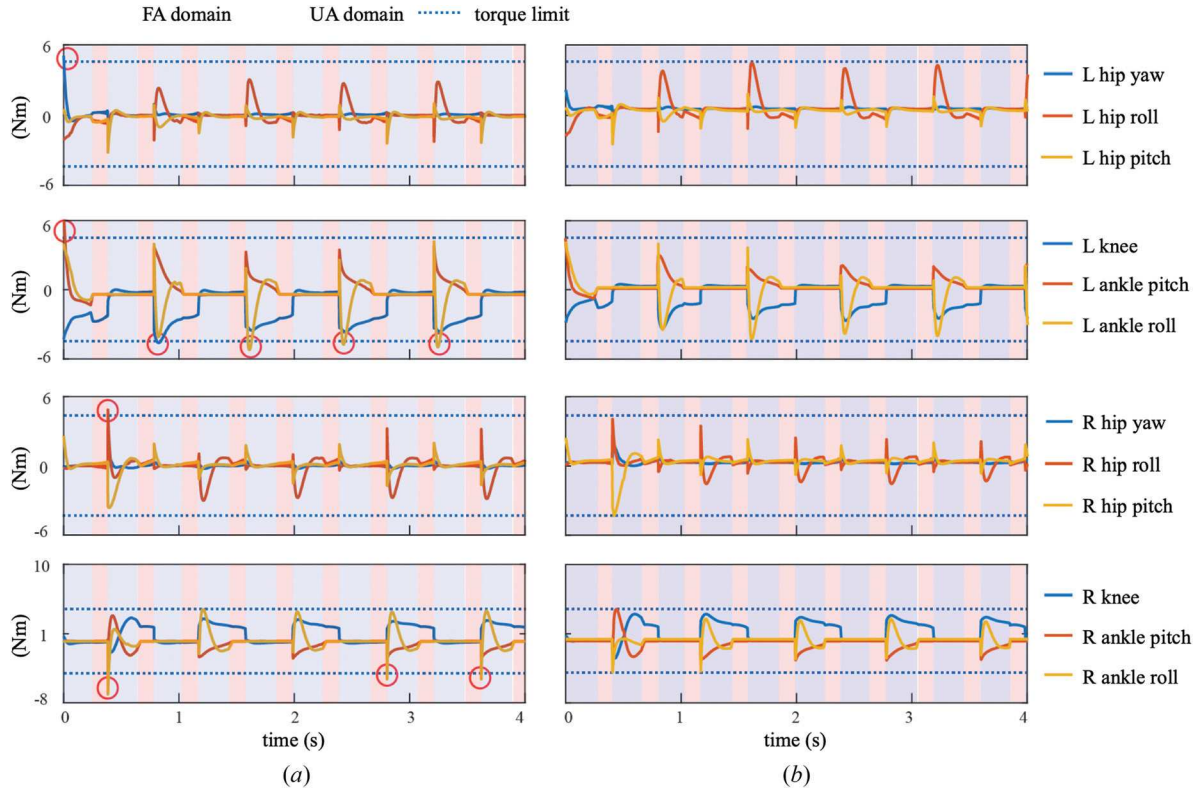

Fig. 12 Torque profiles of each leg motor under the proposed (*a*) IO-PD and (*b*) IO-QP controllers for Case B. "L" and "R" stand for left and right, respectively. The red circles highlight the occurrence of torque limit violations. The torque peaks under the IO-PD controller are more significant than the IO-QP controller because the latter explicitly meets the torque limits. The blue dotted lines represent the torque limits. It is evident that the torque profile of the IO-QP controller adheres to the torque limits, whereas the torque profile of the IO-PD controller may exceed the torque limits.

HZD-based approaches, the global-position control approach designed for underactuated walking [12] is also based on orbital stabilization. Therefore, although the recent global-position control approach [12] can ensure accurate tracking of the desired global path, it may not guarantee the precise timing for tracking a time trajectory along the global path. Still, one distinct advantage of [12] and the HZD-based approaches is that they can provably stabilize underactuated walking, which the proposed approach is not able to achieve in its current form. Our future work will focus on the GPT control of underactuated walking.

Our previous GPT controller design [17] for the multi-domain walking of a 2D robot is only capable of tracking straight-line paths. By explicitly modeling the robot dynamics associated with 3D walking and considering the robot's 3D movement in the design of the desired trajectories, the proposed approach is capable of ensuring satisfactory GPT performance for 3D walking.

One limitation of the proposed approach is that it may be nonfeasible to meet the proposed stability conditions in practice if the duration of the UA phase, δ_{τ_U}, is overly large. From Eq. (A20) in the proof of Proposition 3, we know that as δ_{τ_U} increases, α_2 will also increase, leading to a larger value of $\overline{N}$. If $\overline{N}$ is overly large, Eq. (34) will no longer hold, and the stability conditions will be invalid. To resolve this potential issue, the nominal duration of the UA domain cannot be set overly long. Indeed, the percentage of the UA phase within a complete gait cycle is respectively 8% and 19% of the simulated three-domain and two-domain walking. Thanks to the explicit dependence of the Lyapunov-like function V_U on the state variable, we can obtain the upper bound of the UA phase duration corresponding to the bound of the Lyapunov-like function V_U. Specifically, we could use the inequalities in Eqs. (A5) and (A6) to determine the upper bound of the UA duration defined by the small number ε_U. Since the bound of the Lyapunov-like function V_U also depends on ε_U, we can then translate this bound onto the UA duration bound through ε_U. While the percentage of the UA phase within a complete two-domain gait cycle is 19% and comparable to that of human walking (i.e., 18% [1,37]), the UA phase percentage of the three-domain walking, 8%, is notably lower. We hypothesize that how much we can maximize the UA percentage of three-domain walking largely depends on the configuration of OP3's proprietary foot design. OP3 has one-piece, highly stiff feet, which are typically suitable for single-domain walking such as fully actuated walking, instead of multi-domain walking that involves support-foot rolling.

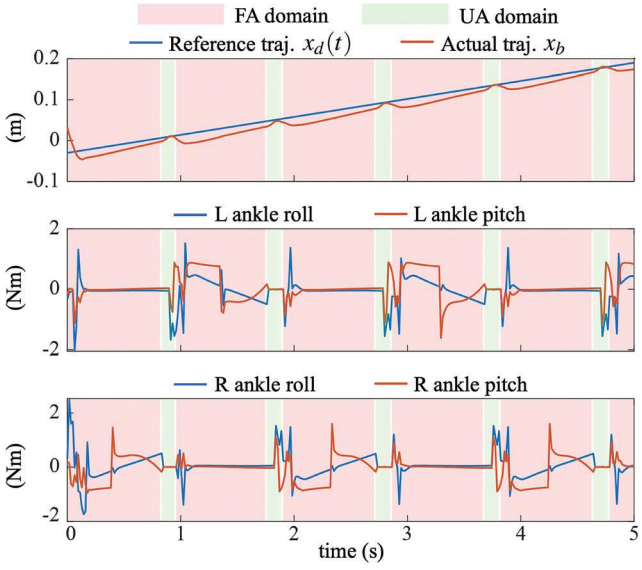

Fig. 13 Two-domain walking results in 3D realistic Webots simulation under the proposed IO-QP controller. "L" and "R" stand for left and right, respectively. The UA phase is approximately 16% of a gait cycle. The global-position tracking error remains small, and the ankle torque is well bounded.

Thanks to its small surface contact at the toe and the heel, the foot design of the AMBER2 robot [1] mentioned earlier is more suitable for multi-domain walking than OP3. Inspired by the success of Zhao et al. [1], our future experiments will incorporate such a foot design modification of commercial robot platforms (e.g., the OP3 robot used in this study). Our future work will also redesign the output functions to indirectly regulate the divergence rate during the UA phase. For input-output linearizing control [6,29], the internal dynamics or zero dynamics during a UA phase cannot be directly controlled. Yet, the definition of the output function will impact the expression of the zero dynamics and thus affect its stability and convergence/divergence rate. Thus, similar to Westervelt et al. and Gu et al. [6,19], we can parameterize the output functions as Beziér polynomials and optimize the Beziér coefficients to reduce the divergence rate or even achieve convergence for the underactuation phase. Note that this optimization method is theoretically valid for general multi-domain walking involving underactuation, including both two-domain and three-domain walking.

Another limitation of our control laws lies in that the robot dynamics model needs to be sufficiently accurate for the controller to be effective, due to the utilization of the input-output linearization technique. Yet, model parametric errors, external disturbances, and hardware imperfections (e.g., sensor noise) are prevalent in real-world robot operations [38]. To address this issue for our future hardware experiments, a common solution is to employ a joint-level PD controller [6]. Although the actual PD controller implemented on hardware is not exactly the theoretically derived input-output linearizing controller, the actual controller can still be effective for two main reasons. First, the desired joint-level trajectories that the PD controller tracks are typically obtained by using the robot's full-order inverse kinematics model to translate the desired task-space trajectories into the configuration space [20]. This translation preserves the agreement of the desired trajectories with the system dynamics and feasibility conditions. Second, the joint-level PD controller is by nature a feedback controller and thus has its inherent robustness against a certain range of uncertainties. From previous studies [6] and our work [20,23], it has been proven that the inherent robustness of the joint-level PD control with appropriate controller parameters can mitigate a reasonable level of real-world uncertainties for ensuring stable fully actuated and underactuated walking on physical bipedal robot platforms. To further enhance the robustness of the proposed controller for real-world applications, we can incorporate robust control [22,39–41] into the GPT control law to address uncertainties. Furthermore, we can exploit online footstep planning [12,36,42–45] to adjust the robot's desired behaviors in real-time to better reject modeling errors and external disturbances.

8 Conclusion

This paper has introduced a continuous tracking control law that achieves provably accurate global-position tracking for the hybrid model of multi-domain bipedal robotic walking involving different actuation types. The proposed control law was derived based on input-output linearization and proportional-derivative control, ensuring the exponential stability of the output function dynamics within each continuous phase of the hybrid walking process. Sufficient stability conditions were established via the construction of multiple Lyapunov functions and could be used to guide the gain tuning of the proposed control law for ensuring the provable stability for the overall hybrid system. Both a three-domain and a two-domain walking gait were investigated to illustrate the effectiveness of the proposed approach, and the input-output linearizing controller was cast into a quadratic program to handle the actuator torque saturation. Simulation results on a three-dimensional bipedal humanoid robot confirmed the validity of the proposed control law under a variety of walking paths, desired global-position trajectories, desired walking patterns, and initial errors. Finally, the performance of the input-output linearizing control law with and without the quadratic program formulation was compared to highlight the effectiveness of the former in mitigating torque

saturation while ensuring the closed-loop stability and trajectory tracking accuracy.

Acknowledgment

The authors would like to thank Sushant Veer and Ayonga Hereid for their constructive comments on the theory and simulations of this work.

Funding Data

- Division of Civil, Mechanical and Manufacturing Innovation, National Science Foundation (Grant No. 1934280; Funder ID: 10.13039/100000147).

Data Availability Statement

The datasets generated and supporting the findings of this article are obtainable from the corresponding author upon reasonable request.

Appendix: Proofs of Propositions and Theorem 1

A.1 Proof of Proposition 2. Integrating both sides of the UA closed-loop dynamics in Eq. (24) over time t yields

$$\mathbf{x}_\eta|_{3k-1}^- = \int_{T_{3k-2}}^{T_{3k-1}} \mathbf{f}_\eta\big(s, \mathbf{x}_\eta(s), \mathbf{x}_\xi(s)\big) ds + \mathbf{x}_\eta|_{3k-2}^+ \tag{A1}$$

Then

$$\begin{aligned} ||\mathbf{x}_\eta|_{3k-1}^-|| &\le ||\int_{T_{3k-2}}^{T_{3k-1}} \mathbf{f}_\eta\big(s, \mathbf{x}_\eta(s), \mathbf{x}_\xi(s)\big) ds|| + ||\mathbf{x}_\eta|_{3k-2}^+|| \\ &\le \int_{T_{3k-2}}^{T_{3k-1}} ||\mathbf{f}_\eta\big(s, \mathbf{x}_\eta(s), \mathbf{x}_\xi(s)\big)|| ds + ||\mathbf{x}_\eta|_{3k-2}^+|| \end{aligned} \tag{A2}$$

Since the expression of $\mathbf{f}_\eta(\cdot)$ is obtained using the continuous-phase dynamics of the generalized coordinates in Eq. (4) and the expression of the output function $\mathbf{y}_U$ in Eqs. (17) and (18), we know $\mathbf{f}_\eta(t, \mathbf{x}_\eta, \mathbf{x}_\xi)$ is continuously differentiable in t, $\mathbf{x}_\eta$, and $\mathbf{x}_\xi$. Also, we can prove that there exists a finite, real, positive number r_η such that $||\frac{\partial \mathbf{f}_\eta}{\partial t}||$, $||\frac{\partial \mathbf{f}_\eta}{\partial \mathbf{x}_\xi}||$, and $||\frac{\partial \mathbf{f}_\eta}{\partial \mathbf{x}_\eta}||$ are bounded on $(T_{3k-2}, T_{3k-1}) \times B_{r_\eta}(\mathbf{0})$. Then, $\mathbf{f}_\eta(t, \mathbf{x}_\eta, \mathbf{x}_\xi)$ is Lipschitz continuous on $(T_{3k-2}, T_{3k-1}) \times B_{r_\eta}(\mathbf{0})$ [29], and we can prove there exists a real, positive number k_f such that

$$||\mathbf{f}_\eta\big(t, \mathbf{x}_\eta(t), \mathbf{x}_\xi(t)\big)|| \le k_f \tag{A3}$$

holds for any $t \times (\mathbf{x}_\eta, \mathbf{x}_\xi) \in (T_{3k-2}, T_{3k-1}) \times B_{r_\eta}(\mathbf{0})$.

Combining the two inequalities above, we have

$$||\mathbf{x}_\eta|_{3k-1}^-|| \le k_f(T_{3k-1} - T_{3k-2}) + ||\mathbf{x}_\eta|_{3k-2}^+|| \tag{A4}$$

The duration $(T_{3k-1} - T_{3k-2})$ of the UA phase can be estimated as

$$\begin{aligned} |T_{3k-1} - T_{3k-2}| &= |T_{3k-1} - \tau_{3k-1} + \tau_{3k-1} - T_{3k-2}| \\ &\le |T_{3k-1} - \tau_{3k-1}| + \delta_{\tau_U} \end{aligned} \tag{A5}$$

where $\delta_{\tau_U} := \tau_{3k-1} - T_{3k-2}$ is the expected duration of the UA phase and $|T_{3k-1} - \tau_{3k-1}|$ is the absolute difference between the actual and planned time instants of the UA→OA switching.

From our previous work [20], we know there exists small positive numbers ϵ_U and r_{U1} such that

$$|T_{3k-1} - \tau_{3k-1}| \le \epsilon_U \delta_{\tau_U} \tag{A6}$$

holds for any $k \in \{1, 2, \ldots\}$ and $\mathbf{x}_U \in B_{r_{U1}}(\mathbf{0})$.

Thus, using Eqs. (A4)–(A6), we have

$$||\mathbf{x}_\eta|_{3k-1}^-|| \le k_f(1 + \epsilon_U)\delta_{\tau_U} + ||\mathbf{x}_\eta|_{3k-2}^+|| \tag{A7}$$

Substituting Eqs. (30) and (A7) into Eq. (26) gives

$$\begin{aligned} V_U|_{3k-1}^- &= V_\xi|_{3k-1}^+ + \beta||\mathbf{x}_\eta|_{3k-1}^+||^2 \\ &\le e^{-c_{3\xi}(T_{3k-1} - T_{3k-2})} V_\xi|_{3k-2}^+ + \beta||\mathbf{x}_\eta|_{3k-2}^+||^2 \\ &\quad + 2\beta k_f^2(1 + \epsilon_U)^2 \delta_{\tau_U}^2 \\ &\le V_U|_{3k-2}^+ + 2\beta k_f^2(1 + \epsilon_U)^2 \end{aligned} \tag{A8}$$

Thus, for any $\mathbf{x}_U \in B_{r_{U2}}(\mathbf{0})$ with $r_{U2} := \min(r_\eta, r_{U1})$

$$V_U|_{3k-1}^- \le w_u\big(V_U|_{3k-2}^+\big)$$

holds, where $w_u\big(V_U|_{3k-2}^+\big) := V_U|_{3k-2}^+ + 2\beta k_f^2(1 + \epsilon_U)^2$. Clearly, $w_u\big(V_U|_{3k-2}^+\big)$ is a positive-definite function.

A.2 Proof of Proposition 3. For brevity, we only show the proof for $\ldots \le V_F|_{3k}^+ \le V_F|_{3k-3}^+ \le \ldots \le V_F|_3^+ \le V_F|_0^+$, based on which the proofs for the rest inequalities in Eq. (34) can be readily obtained.

To prove that $V_F|_{3k}^+ \le V_F|_{3k-3}^+$ for any $k \in \{1, 2, \ldots\}$, we need to analyze the evaluation of the state variables for the k^{th} actual complete gait cycle on $t \in (T_{3k-3}, T_{3k})$, which comprises three continuous phases and three switching events.

• **Analyzing the Continuous-Phase State Evolution:** We analyze the state evolution during the three continuous phases based on the convergence and boundedness results established in Propositions 1 and 2.

Similar to the boundedness of the UA→OA switching time discrepancy given in Eq. (A6), there exist small positive numbers ε_F, ε_O, r_{tF}, and r_{tO} such that for any $\mathbf{x}_F \in \mathbf{B}_{r_{tF}}(\mathbf{0})$ and $\mathbf{x}_O \in \mathbf{B}_{r_{tO}}(\mathbf{0})$

$$|T_{3k-2} - \tau_{3k-2}| \le \epsilon_F \delta_{\tau_F} \text{ and } |T_{3k} - \tau_{3k}| \le \epsilon_O \delta_{\tau_O} \tag{A9}$$

hold, where δ_{τ_F} and δ_{τ_O} are the desired periods of the FA and OA phases of the planned walking cycle, with $\delta_{\tau_F} := \tau_{3k-2} - T_{3k-3}$ and $\delta_{\tau_O} := \tau_{3k} - T_{3k-1}$.

Substituting Eq. (A9) into Eqs. (28) and (29) yields

$$||\mathbf{x}_F|_{3k-2}^-|| \le \sqrt{\frac{c_{2F}}{c_{1F}}} e^{-\frac{c_{3F}}{2c_{2F}}(1+\epsilon_F)\delta_{\tau_F}} ||\mathbf{x}_F|_{3k-3}^+|| \tag{A10}$$

and

$$||\mathbf{x}_O|_{3k}^-|| \le \sqrt{\frac{c_{2O}}{c_{1O}}} e^{-\frac{c_{3O}}{2c_{2O}}(1+\epsilon_O)\delta_{\tau_O}} ||\mathbf{x}_O|_{3k-1}^+|| \tag{A11}$$

for any $\mathbf{x}_i \in B_{\bar{r}_i}(\mathbf{0})$ $(i \in \{F, O\})$, with the small positive number $\bar{r}_i$ defined as $\bar{r}_i := \min\{r_i, r_{ti}\}$.

From the definition of the Lyapunov-like function V_U in Eq. (26), the continuous-phase boundedness of V_U in Eq. (A8), and the continuous-phase convergence of V_ξ in Eq. (30), we obtain the following inequality characterizing the boundedness of the state $\mathbf{x}_U$ within the UA phase:

$$||\mathbf{x}_U|_{3k-1}^-||^2 \le 2\frac{\tilde{c}_{2\xi}}{\tilde{c}_{1\xi}} ||\mathbf{x}_U|_{3k-2}^+||^2 + \frac{2\beta k_f^2}{\tilde{c}_{1\xi}}(1 + \epsilon_U)^2 \tag{A12}$$

where the real scalar constants $\tilde{c}_{1\xi}$ and $\tilde{c}_{2\xi}$ are defined as $\tilde{c}_{1\xi} := \min(c_{1\xi}, \beta)$ and $\tilde{c}_{2\xi} := \max(c_{2\xi}, \beta)$.

Since

$$2\frac{\tilde{c}_{2\xi}}{\tilde{c}_{1\xi}}||\mathbf{x}_U|^+_{3k-2}||^2+\frac{2\beta k_f^2}{\tilde{c}_{1\xi}}(1+\epsilon_U)^2 \le\left(\sqrt{2\frac{\tilde{c}_{2\xi}}{\tilde{c}_{1\xi}}}||\mathbf{x}_U|^+_{3k-2}||+\sqrt{\frac{2\beta k_f^2}{\tilde{c}_{1\xi}}}(1+\epsilon_U)\right)^2$$

we rewrite Eq. (A12) as

$$\begin{aligned}||\mathbf{x}_U|^-_{3k-1}|| &\le \sqrt{2\frac{\tilde{c}_{2\xi}}{\tilde{c}_{1\xi}}}||\mathbf{x}_U|^+_{3k-2}||+\sqrt{\frac{2\beta k_f^2}{\tilde{c}_{1\xi}}}(1+\epsilon_U)\\ &=:\alpha_1||\mathbf{x}_U|^+_{3k-2}||+\alpha_2\end{aligned} \tag{A13}$$

• **Analyzing the State Evolution Across a Jump:** Without loss of generality, we first examine the state evolution across the F→U switching event by relating the norms of the state variable just before and after the impact.

Using the expression of the reset map $\mathbf{\Delta}_{F\to U}$ at the switching instant $t=T^-_{3k-2}$ ($k\in\{1,2,\ldots\}$), we obtain the following inequality:

$$\begin{aligned}||\mathbf{x}_U|^+_{3k-2}|| &= ||\mathbf{\Delta}_{F\to U}\left(T_{3k-2},\mathbf{x}_F|^-_{3k-2}\right)||\\ &= ||\left(\mathbf{\Delta}_{F\to U}\left(T_{3k-2},\mathbf{x}_F|^-_{3k-2}\right)-\mathbf{\Delta}_{F\to U}\left(\tau_{3k-2},\mathbf{x}_F|^-_{3k-2}\right)\right)\\ &\quad+\left(\mathbf{\Delta}_{F\to U}\left(\tau_{3k-2},\mathbf{x}_F|^-_{3k-2}\right)-\mathbf{\Delta}_{F\to U}(\tau_{3k-2},\mathbf{0})\right)\\ &\quad+\mathbf{\Delta}_{F\to U}(\tau_{3k-2},\mathbf{0})||\\ &\le ||\mathbf{\Delta}_{F\to U}\left(T_{3k-2},\mathbf{x}_F|^-_{3k-2}\right)-\mathbf{\Delta}_{F\to U}\left(\tau_{3k-2},\mathbf{x}_F|^-_{3k-2}\right)||\\ &\quad+||\mathbf{\Delta}_{F\to U}\left(\tau_{3k-2},\mathbf{x}_F|^-_{3k-2}\right)-\mathbf{\Delta}_{F\to U}(\tau_{3k-2},\mathbf{0})||\\ &\quad+||\mathbf{\Delta}_{F\to U}(\tau_{3k-2},\mathbf{0})||\end{aligned} \tag{A14}$$

Next, we relate the three terms on the right-hand side of the inequality in Eq. (A14) explicitly with the norm of the state just before the switching (i.e., $\mathbf{x}_F|^-_{3k-2}$).

Recall that the expressions of $\mathbf{\Delta}_{F\to U}(t,\mathbf{x}_F)$ solely depends on the expressions of: (i) the impact dynamics $\mathbf{\Delta}_{\dot{q}}(\mathbf{q})\dot{\mathbf{q}}$, which is continuously differentiable on $(\mathbf{q},\dot{\mathbf{q}})\in\mathcal{TQ}$; (ii) the output functions $\mathbf{y}_F(t,\mathbf{q})$, which is continuously differentiable on $t\in\mathbb{R}^+$ and $\mathbf{q}\in\mathcal{Q}$ under assumption (A7); and (iii) the time derivative $\dot{\mathbf{y}}_F(t,\mathbf{q},\dot{\mathbf{q}})$, which, also under assumption (A7), is continuously differentiable on $t\in\mathbb{R}^+$ and $(\mathbf{q},\dot{\mathbf{q}})\in\mathcal{TQ}$. Thus, we know $\mathbf{\Delta}_{F\to U}$ is continuously differentiable for any $t\in\mathbb{R}^+$ (i.e., including any continuous phases) and state $\mathbf{x}_F\in\mathbb{R}^{2n}$.

Similarly, under assumption (A7), we can prove that there exists a small, real constant $_{l_F}$ such that $||\frac{\partial\mathbf{\Delta}_{F\to U}}{\partial t}||$ and $||\frac{\partial\mathbf{\Delta}_{F\to U}}{\partial\mathbf{x}_F}||$ are bounded for any $t\in\mathbb{R}^+$ (including all continuous FA phases) and $\mathbf{x}_F\in B_{l_F}(\mathbf{0})$. Thus, for any $k\in\{1,2,\ldots\}$, the function $\mathbf{\Delta}_{F\to U}$ is Lipschitz continuous for any $t\in[T_{3k-2};\tau_{3k-2}]$ and $\mathbf{x}_F\in B_{l_F}(\mathbf{0})$, where $[T_{3k-2};\tau_{3k-2}]$ equals $[T_{3k-2},\tau_{3k-2}]$ if $T_{3k-2}<\tau_{3k-2}$, and it equals $[\tau_{3k-2},T_{3k-2}]$ if $T_{3k-2}>\tau_{3k-2}$.

Then, there exist Lipschitz constants L_{tF} and L_{xF} such that

$$\begin{aligned}&||\mathbf{\Delta}_{F\to U}\left(T_{3k-2},\mathbf{x}_F|^-_{3k-2}\right)-\mathbf{\Delta}_{F\to U}\left(\tau_{3k-2},\mathbf{x}_F|^-_{3k-2}\right)||\\ \le& L_{tF}|T_{3k-2}-\tau_{3k-2}|\end{aligned} \tag{A15}$$

and

$$||\mathbf{\Delta}_{F\to U}\left(\tau_{3k-2},\mathbf{x}_F|^-_{3k-2}\right)-\mathbf{\Delta}_{F\to U}(\tau_{3k-2},\mathbf{0})||\le L_{xF}||\mathbf{x}_F|^-_{3k-2}|| \tag{A16}$$

hold on $[T_{3k-2};\tau_{3k-2}]\times B_{l_F}(\mathbf{0})$ for any $k\in\{1,2,\ldots\}$.

From condition (A2) and Eqs. (31), (A9), and (A14)–(A16), we know that

$$||\mathbf{x}_U|^+_{3k-2}||\le L_{xF}||\mathbf{x}_F|^-_{3k-2}||+L_{tF}\epsilon_F\delta_{\tau F}+\gamma_\Delta \tag{A17}$$

Analogous to the derivation of the inequality in Eq. (A17), we can show that there exist a real, positive number l_U and Lipschitz constants L_{tU} and L_{xU} such that

$$||\mathbf{x}_O|^+_{3k-1}||\le L_{xU}||\mathbf{x}_U|^-_{3k-1}||+L_{tU}\epsilon_U\delta_{\tau_U}+\gamma_\Delta \tag{A18}$$

holds for any $\mathbf{x}_U|^-_{3k-1}\in B_{l_U}(\mathbf{0})$.

As the robot has full control authority within the OA domain, we can establish a tighter upper bound on $||\mathbf{x}_F|^+_{3k}||$ than Eqs. (A17) and (A18) by applying Proposition 3 from our previous work [23]. That is, there exists a real, positive number l_O and Lipschitz constants L_{tO} and L_{xO} such that

$$||\mathbf{x}_F|^+_{3k}||\le L_{tO}\sqrt{\frac{c_{2O}}{c_{1O}}}e^{-\frac{c_{3O}}{2c_{2O}}\delta_{\tau_O}}||\mathbf{x}_O|^+_{3k-1}||+L_{xO}||\mathbf{x}_O|^-_{3k}|| \tag{A19}$$

for any $\mathbf{x}_O|^-_{3k}\in B_{l_O}(\mathbf{0})$.

From Eqs. (A10), (A11), (A13), and (A17)–(A19), we obtain

$$||\mathbf{x}_F|^+_{3k}||\le\bar{N}+\bar{L}||\mathbf{x}_F|^+_{3k-3}|| \tag{A20}$$

where

$$\begin{aligned}\bar{N}:=&(L_{tU}\epsilon_U\delta_{\tau_U}+\gamma_\Delta+L_{xU}(\alpha_1L_{tF}\epsilon_F\delta_{\tau_F}+\alpha_1\gamma_\Delta+\alpha_1\alpha_2))\\ &\cdot\left(L_{tO}\sqrt{\frac{c_{2O}}{c_{1O}}}e^{-\frac{c_{3O}}{2c_{2O}}\delta_{\tau_O}}+L_{xO}\sqrt{\frac{c_{2O}}{c_{1O}}}e^{-\frac{c_{3O}}{2c_{2O}}(1+\epsilon_O)\delta_{\tau_O}}\right)\end{aligned}$$

and

$$\begin{aligned}\bar{L}:=&L_{xU}\alpha_1L_{xF}\sqrt{\frac{c_{2F}}{c_{1F}}}e^{-\frac{c_{3F}}{2c_{2F}}(1+\epsilon_F)\delta_{\tau_F}}\\ &\cdot\left(L_{tO}\sqrt{\frac{c_{2O}}{c_{1O}}}e^{-\frac{c_{3O}}{2c_{2O}}\delta_{\tau_O}}+L_{xO}\sqrt{\frac{c_{2O}}{c_{1O}}}e^{-\frac{c_{3O}}{2c_{2O}}(1+\epsilon_O)\delta_{\tau_O}}\right)\end{aligned}$$

Using Eqs. (27) and (A20), we obtain

$$V_F|^+_{3k}\le 2c_{2F}\bar{N}^2+\frac{2c_{2F}\bar{L}^2}{c_{1F}}V_F|^+_{3k-3} \tag{A21}$$

Note that the scalar positive parameters $\bar{N}$ and $\bar{L}$ in Eq. (A21) are both dependent on the continuous-phase convergence rates of the Lyapunov-like functions within the OA and FA domains (i.e., c_{3F} and c_{3O}), Specifically, $\bar{N}$ and $\bar{L}$ (and accordingly $\frac{2c_{2F}\bar{L}^2}{c_{1F}}$ and $2c_{2F}\bar{N}^2$) will decrease toward zero as the continuous-phase convergence rates increase toward the infinity.

If condition (A3) holds (i.e., the PD gains can be adjusted to ensure a sufficiently high continuous-phase convergence rate), we can choose the PD gains such that $\frac{2c_{2F}\bar{L}^2}{c_{1F}}$ is less than 1 and $2c_{2F}\bar{N}^2$ is sufficiently close to 0, which will then ensure $V_F|^+_{3k}\le V_F|^+_{3k-3}$ for any $k\in\{1,2,\ldots\}$.

A.3 Proof of Theorem 1. By the general stability theory based on multiple Lyapunov functions [31], the origin of the overall hybrid error system described in Eqs. (22) and (24) is locally stable in the sense of Lyapunov if the Lyapunov-like functions V_F, V_O, and V_U satisfy the following conditions:

(C1) The Lyapunov-like functions V_F and V_O exponentially decrease within the continuous FA and OA phases, respectively.

(C2) Within the continuous UA phase, the "switching-out" value of the Lyapunov-like function V_U is bounded above by a positive-definite function of the "switching-in" value of V_U; and
(C3) The values of each Lyapunov-like functions at their associated "switching-in" instants form a nonincreasing sequence.

If the proposed IO-PD control law satisfies condition (B1), then the control law ensures conditions (C1) and (C2), as established in Proposition 1 and 2, respectively. By further meeting conditions (B2) and (B3), we know from Proposition 3 that condition (C3) will hold. Thus, under conditions (B1)–(B3), the closed-loop control system meets conditions (C1)–(C3), and the origin of the overall hybrid error system described in Eqs. (22) and (23) is locally stable in the sense of Lyapunov.

■

References

[1] Zhao, H., Hereid, A., Ma, W-L., and Ames, A. D., 2017, "Multi-Contact Bipedal Robotic Locomotion," Robotica, **35**(5), pp. 1072–1106.
[2] Zhao, H.-H., Ma, W.-L., Ames, A. D., and Zeagler, M. B., 2014, "Human-Inspired Multi-Contact Locomotion With AMBER2," ACM/IEEE International Conference on Cyber-Physical Systems (ICCPS), Berlin, Germany, Apr. 14–17, pp. 199–210.
[3] Ramezani, A., Hurst, J. W., Hamed, K. A., and Grizzle, J. W., 2014, "Performance Analysis and Feedback Control of ATRIAS, A Three-Dimensional Bipedal Robot," ASME J. Dyn. Syst. Meas. Control, **136**(2), p. 021012.
[4] Hereid, A., Kolathaya, S., Jones, M. S., Van Why, J., Hurst, J. W., and Ames, A. D., 2014, "Dynamic Multi-Domain Bipedal Walking With Atrias Through SLIP Based Human-Inspired Control," Proceedings of International Conference on Hybrid Systems: Computation and Control, Berlin, Germany, Apr. 14–17, pp. 263–272.
[5] Schwind, W. J., 1998, *Spring Loaded Inverted Pendulum Running: A Plant Model*, University of Michigan, Ann Arbor, MI.
[6] Westervelt, E. R., Chevallereau, C., Choi, J. H., Morris, B., and Grizzle, J. W., 2007, *Feedback Control of Dynamic Bipedal Robot Locomotion*, CRC Press, Boca Raton, FL.
[7] Reher, J., Cousineau, E. A., Hereid, A., Hubicki, C. M., and Ames, A. D., 2016, "Realizing Dynamic and Efficient Bipedal Locomotion on the Humanoid Robot DURUS," IEEE International Conference on Robotics and Automation, Stockholm, Sweden, May 16–21, pp. 1794–1801.
[8] Hamed, K. A., Ma, W.-L., and Ames, A. D., 2019, "Dynamically Stable 3D Quadrupedal Walking With Multi-Domain Hybrid System Models and Virtual Constraint Controllers," American Control Conference (ACC), Philadelphia, PA, July 10–12, pp. 4588–4595.
[9] Hamed, K., Safaee, B., and Gregg, R. D., 2019, "Dynamic Output Controllers for Exponential Stabilization of Periodic Orbits for Multidomain Hybrid Models of Robotic Locomotion," ASME J. Dyn. Syst. Meas. Control, **141**(12), p. 121011.
[10] Grizzle, J. W., Abba, G., and Plestan, F., 2001, "Asymptotically Stable Walking for Biped Robots: Analysis Via Systems With Impulse Effects," IEEE Trans. Autom. Control, **46**(1), pp. 51–64.
[11] Xiong, X., Reher, J., and Ames, A. D., 2021, "Global Position Control on Underactuated Bipedal Robots: Step-to-Step Dynamics Approximation for Step Planning," IEEE International Conference on Robotics and Automation (ICRA), Xi'an, China, May 30–June 5, pp. 2825–2831.
[12] Xiong, X., and Ames, A., 2022, "3-D Underactuated Bipedal Walking Via H-LIP Based Gait Synthesis and Stepping Stabilization," IEEE Trans. Rob., **38**(4), pp. 2405–2425.
[13] Dai, M., Lee, J., and Ames, A. D., 2023, "Multi-Domain Walking With Reduced-Order Models of Locomotion," arXiv:2310.03179.
[14] Westervelt, E. R., Grizzle, J. W., and Koditschek, D. E., 2003, "Hybrid Zero Dynamics of Planar Biped Walkers," IEEE Trans. Autom. Control, **48**(1), pp. 42–56.
[15] Sreenath, K., Park, H.-W., Poulakakis, I., and Grizzle, J. W., 2011, "A Compliant Hybrid Zero Dynamics Controller for Stable, Efficient and Fast Bipedal Walking on MABEL," Int. J. Rob. Res., **30**(9), pp. 1170–1193.
[16] Gong, Y., Hartley, R., Da, X., Hereid, A., Harib, O., Huang, J.-K., and Grizzle, J., 2019, "Feedback Control of a Cassie Bipedal Robot: Walking, Standing, and Riding a Segway," American Control Conference (ACC), Philadelphia, PA, July 10–12, pp. 4559–4566.
[17] Gu, Y., Yao, B., and Lee, C. G., 2016, "Bipedal Gait Recharacterization and Walking Encoding Generalization for Stable Dynamic Walking," IEEE International Conference on Robotics and Automation (ICRA), Stockholm, Sweden, May 16–21, pp. 1788–1793.
[18] Gu, Y., Yao, B., and Lee, C. G., 2018, "Straight-Line Contouring Control of Fully Actuated 3-D Bipedal Robotic Walking," American Control Conference (ACC), Milwaukee, WI, June 27–29, pp. 2108–2113.
[19] Gu, Y., Yao, B., and Lee, C. G., 2017, "Time-Dependent Orbital Stabilization of Underactuated Bipedal Walking," American Control Conference (ACC), Seattle, WA, May 24–26, pp. 4858–4863.
[20] Gao, Y., and Gu, Y., 2019, "Global-Position Tracking Control of a Fully Actuated NAO Bipedal Walking Robot," American Control Conference (ACC), Philadelphia, PA, July 10–12, pp. 4596–4601.
[21] Gu, Y., and Yuan, C., 2020, "Adaptive Robust Trajectory Tracking Control of Fully Actuated Bipedal Robotic Walking," IEEE/ASME International Conference on Advanced Intelligent Mechatronics (AIM), Boston, MA, July 6–9, pp. 1310–1315.
[22] Gu, Y., and Yuan, C., 2021, "Adaptive Robust Tracking Control for Hybrid Models of Three-Dimensional Bipedal Robotic Walking Under Uncertainties," ASME J. Dyn. Syst. Meas. Control, **143**(8), p. 081007.
[23] Gu, Y., Gao, Y., Yao, B., and Lee, C. G., 2022, "Global-Position Tracking Control for Three-Dimensional Bipedal Robots Via Virtual Constraint Design and Multiple Lyapunov Analysis," ASME J. Dyn. Syst. Meas. Control, **144**(11), p. 111001.
[24] Iqbal, A., and Gu, Y., 2021, "Extended Capture Point and Optimization-Based Control for Quadrupedal Robot Walking on Dynamic Rigid Surfaces," IFAC-PapersOnLine, **54**(20), pp. 72–77.
[25] Iqbal, A., Gao, Y., and Gu, Y., 2020, "Provably Stabilizing Controllers for Quadrupedal Robot Locomotion on Dynamic Rigid Platforms," IEEE/ASME Trans. Mechatron., **25**(4), pp. 2035–2044.
[26] Iqbal, A., Veer, S., and Gu, Y., 2023, "Real-Time Walking Pattern Generation of Quadrupedal Dynamic-Surface Locomotion Based on a Linear Time-Varying Pendulum Model," arXiv:2301.03097.
[27] Gao, Y., and Gu, Y., 2019, "Global-Position Tracking Control of Multi-Domain Planar Bipedal Robotic Walking," ASME Paper No. DSCC2019-9117.
[28] Bhounsule, P. A., and Zamani, A., 2017, "A Discrete Control Lyapunov Function for Exponential Orbital Stabilization of the Simplest Walker," ASME J. Mech. Rob., **9**(5), p. 051011.
[29] Khalil, H. K., 1996, *Nonlinear Systems*, Prentice Hall, New York.
[30] Chan, W. K., Gu, Y., and Yao, B., 2018, "Optimization of Output Functions With Nonholonomic Virtual Constraints in Underactuated Bipedal Walking Control," Annual American Control Conference (ACC), Milwaukee, WI, June 27–29, pp. 6743–6748.
[31] Branicky, M. S., 1998, "Multiple Lyapunov Functions and Other Analysis Tools for Switched and Hybrid Systems," IEEE Trans. Autom. Control, **43**(4), pp. 475–482.
[32] Khalil, H. K., 1996, *Nonlinear Control*, Prentice Hall, New York.
[33] Gu, Y., 2017, "Time-Dependent Nonlinear Control of Bipedal Robotic Walking," Ph.D. thesis, Purdue University.
[34] Rijnen, M., Biemond, J. B., Van De Wouw, N., Saccon, A., and Nijmeijer, H., 2020, "Hybrid Systems With State-Triggered Jumps: Sensitivity-Based Stability Analysis With Application to Trajectory Tracking," IEEE Trans. Autom. Control, **65**(11), pp. 4568–4583.
[35] Rijnen, M., van Rijn, A., Dallali, H., Saccon, A., and Nijmeijer, H., 2016, "Hybrid Trajectory Tracking for a Hopping Robotic Leg," IFAC-PapersOnLine, **49**(14), pp. 107–112.
[36] Gong, Y., and Grizzle, J. W., 2022, "Zero Dynamics, Pendulum Models, and Angular Momentum in Feedback Control of Bipedal Locomotion," ASME J. Dyn. Syst., Meas., Control, **144**(12), p. 121006.
[37] Reher, J. P., Hereid, A., Kolathaya, S., Hubicki, C. M., and Ames, A. D., 2020, "Algorithmic Foundations of Realizing Multi-Contact Locomotion on the Humanoid Robot DURUS," Algorithmic Foundations of Robotics XII: Proceedings of the Twelfth Workshop on the Algorithmic Foundations of Robotics, San Francisco, CA, Dec. 18–20, pp. 400–415.
[38] Yeatman, M., Lv, G., and Gregg, R. D., 2019, "Decentralized Passivity-Based Control With a Generalized Energy Storage Function for Robust Biped Locomotion," ASME J. Dyn. Syst. Meas. Control, **141**(10), p. 101007.
[39] Hu, C., Yao, B., Wang, Q., Chen, Z., and Li, C., 2011, "Experimental Investigation on High-Performance Coordinated Motion Control of High-Speed Biaxial Systems for Contouring Tasks," Int. J. Mach. Tools Manuf., **51**(9), pp. 677–686.
[40] Liao, J., Chen, Z., and Yao, B., 2017, "High-Performance Adaptive Robust Control With Balanced Torque Allocation for the Over-Actuated Cutter-Head Driving System in Tunnel Boring Machine," Mechatronics, **46**, pp. 168–176.
[41] Yuan, M., Chen, Z., Yao, B., and Liu, X., 2021, "Fast and Accurate Motion Tracking of a Linear Motor System Under Kinematic and Dynamic Constraints: An Integrated Planning and Control Approach," IEEE Trans. Control Syst. Technol., **29**(2), pp. 804–811.
[42] Gao, Y., Gong, Y., Paredes, V., Hereid, A., and Gu, Y., 2023, "Time-Varying ALIP Model and Robust Foot-Placement Control for Underactuated Bipedal Robotic Walking on a Swaying Rigid Surface," American Control Conference (ACC), San Diego, CA, May 31–June 2, pp. 3282–3287.
[43] Iqbal, A., Veer, S., and Gu, Y., 2023, "Asymptotic Stabilization of Aperiodic Trajectories of a Hybrid-Linear Inverted Pendulum Walking on a Dynamic Rigid Surface," American Control Conference (ACC), San Diego, CA, May 31–June 2, pp. 3030–3035.
[44] Dai, M., Xiong, X., and Ames, A., 2022, "Bipedal Walking on Constrained Footholds: Momentum Regulation Via Vertical Com Control," International Conference on Robotics and Automation (ICRA), Philadelphia, PA, May 23–27, pp. 10435–10441.
[45] Nguyen, Q., Da, X., Grizzle, J., and Sreenath, K., 2020, "Dynamic Walking on Stepping Stones With Gait Library and Control Barrier Functions," Algorithmic Foundations of Robotics XII: Proceedings of the Twelfth Workshop on the Algorithmic Foundations of Robotics, San Francisco, CA, Dec. 18–20, pp. 384–399.